



Evidence for anorthositic crust formed on an inner solar system planetesimal

P. Frossard, M. Boyet, A. Bouvier, T. Hammouda, J. Monteux

► To cite this version:

P. Frossard, M. Boyet, A. Bouvier, T. Hammouda, J. Monteux. Evidence for anorthositic crust formed on an inner solar system planetesimal. *Geochemical Perspectives Letters*, 2019, 11, pp.28-32. 10.7185/geochemlet.1921 . hal-02315516

HAL Id: hal-02315516

<https://uca.hal.science/hal-02315516>

Submitted on 14 Oct 2019

HAL is a multi-disciplinary open access archive for the deposit and dissemination of scientific research documents, whether they are published or not. The documents may come from teaching and research institutions in France or abroad, or from public or private research centers.

L'archive ouverte pluridisciplinaire **HAL**, est destinée au dépôt et à la diffusion de documents scientifiques de niveau recherche, publiés ou non, émanant des établissements d'enseignement et de recherche français ou étrangers, des laboratoires publics ou privés.

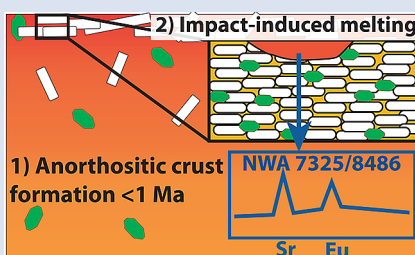
Evidence for anorthositic crust formed on an inner solar system planetesimal

P. Frossard^{1*}, M. Boyet¹, A. Bouvier^{2,3}, T. Hammouda¹, J. Monteux¹



doi: 10.7185/geochemlet.1921

Abstract



During the first million years of solar system history, planetesimals experienced extensive melting powered by the radioactive decay of ^{26}Al (Lee *et al.*, 1977). To date, the only known anorthositic crust on a solar system body is that of the Moon, formed by plagioclase flotation on top of the magma ocean (Wood *et al.*, 1970). Here we show evidence from the ungrouped achondrite meteorite Northwest Africa (NWA) 8486 that an anorthositic crust formed on a planetesimal very early in solar system history (<1.7 Ma). NWA 8486 displays the highest anomalies in Eu and Sr found in achondrites so far and, for the first time, this characteristic is also identified in clinopyroxene. Elemental modelling, together with calculated timescales for crystal settling, show that only the melting of an anorthosite can produce NWA 8486 within the first 5 million years of solar system history. Our results indicate that such a differentiation scenario was achievable over short timescales within the inner solar system, and must have contributed to the making and elemental budget of the terrestrial planets.

Received 18 March 2019 | Accepted 14 August 2019 | Published 7 October 2019

Introduction

Over 80 ungrouped achondrites have been found in the past 20 years, enriching our collections with new types of meteoritic samples. Northwest Africa (NWA) 8486 is one of several paired stones, along with the ungrouped achondrites NWA 7325 and 8014, that have been found in the Sahara desert (Ruzicka *et al.*, 2017). They are plagioclase-rich cumulate gabbros that experienced remelting and fast cooling (Yang *et al.*, 2019), with a very peculiar calcic and magnesian mineralogy. NWA 8486 formed under reduced conditions, with an oxygen fugacity ($f\text{O}_2$) of 3.2 log units below the iron-wüstite (IW) buffer (Sutton *et al.*, 2017), and therefore likely originates from the inner solar system. Based on Cr, Ti and O isotopic compositions, NWA 7325/8486 have affinities with both acapulcoite-lodranite and ureilite groups (Barrat *et al.*, 2015; Weber *et al.*, 2016; Goodrich *et al.*, 2017). The Pb-Pb isochron age of 4563.4 ± 2.6 Ma, Al-Mg age of 4563.09 ± 0.26 Ma and initial Mg isotopic composition for NWA 7325 indicate that the parent material of this meteorite had to be formed within 1–2 Myr after Solar System formation (Koefoed *et al.*, 2016).

Eu and Sr Anomalies in NWA 7325/8486

We investigated major and trace element composition of NWA 8486 through *in situ* and in solution analyses. The mineral compositions of NWA 8486 are consistent with those of NWA

7325 (Barrat *et al.*, 2015; Weber *et al.*, 2016; Goodrich *et al.*, 2017), with $\text{An}_{88.7 \pm 3.0}\text{Ab}_{11.2 \pm 3.0}$ plagioclase, $\text{Wo}_{45.4 \pm 0.5}\text{En}_{53.4 \pm 0.5}\text{Fs}_{1.2 \pm 0.1}$ clinopyroxene and $\text{Fo}_{97.1 \pm 0.3}$ olivine. The modal compositions reported for different fragments of NWA 7325 vary (Barrat *et al.*, 2015; Weber *et al.*, 2016; Goodrich *et al.*, 2017), illustrating the heterogeneous distribution of the minerals at the centimetre scale. The fragment of NWA 8486 studied here contains the highest pyroxene modal content at 52 %, the lowest plagioclase content at 44 %, with the remaining 4 % consisting of olivine, sulphides and metal. The range reported for NWA 7325 is 30–44 % for pyroxene, 54–60 % for plagioclase and 2–15 % for olivine (Barrat *et al.*, 2015; Weber *et al.*, 2016; Goodrich *et al.*, 2017).

We report trace element abundances in mineral (plagioclase, pyroxene and olivine) and a whole rock powder of NWA 8486. Minerals were analysed either *in situ* or in solution after mechanical separation (Supplementary Information). The whole rock composition slightly differs from that of NWA 7325 from Barrat *et al.* (2015) as a consequence of different modal compositions (Fig. 1). Incompatible and moderately volatile elements are depleted in this meteorite, below $0.5 \times \text{CI}$ chondrites for the whole rock with the exceptions of Eu and Sr. Positive Eu and Sr anomalies (Eu/Eu^* and Sr/Sr^*) are present in each mineral phase with different magnitudes, from 1.8 to 6.5 in pyroxene and 450 to 1039 in plagioclase (Supplementary Information). Their amplitude in the whole rock is much higher than that measured in lunar anorthosites (Fig. 1).

1. Université Clermont Auvergne, CNRS, IRD, OPGC, Laboratoire Magmas et Volcans, F-63000 Clermont-Ferrand, France
2. Department of Earth Sciences, Centre for Planetary Science and Exploration, University of Western Ontario, Ontario, Canada
3. Bayerisches Geoinstitut, Universität Bayreuth, Germany
* Corresponding author (email: paul.frossard@uca.fr)



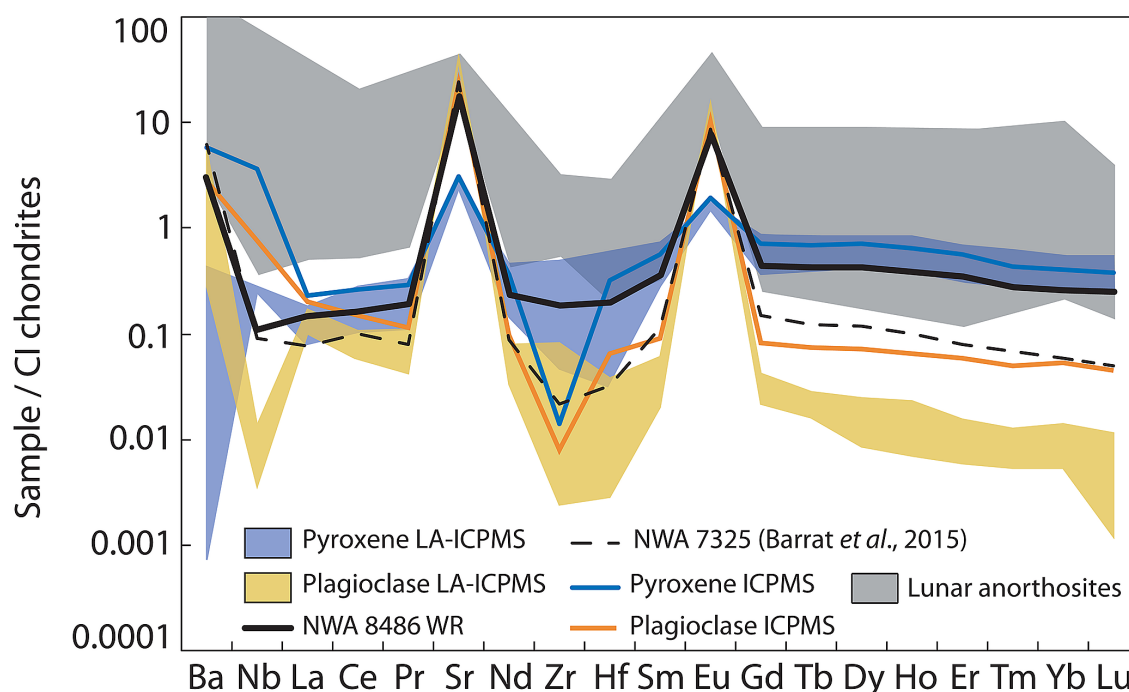


Figure 1 Trace element composition of NWA 8486 normalised to CI chondrites (Anders and Grevesse, 1989). All fractions exhibit Eu and Sr positive anomalies. NWA 7325 has a lower content for most incompatible elements compared to NWA 8486 owing to its modal enrichment in plagioclase. Lunar anorthosites are reported for comparison (data from Haskin *et al.*, 1973 and Norman *et al.*, 2003).

Europium changes valence in a continuum from a 3+ state to a 2+ state around the IW buffer (where $\text{Eu}^{3+}/\Sigma\text{Eu} = 0.5$) and in these conditions plagioclase preferentially incorporates Eu^{2+} in its lattice, resulting in an enrichment in Eu over the other trivalent rare earth elements (REE^{3+}). The similar plagioclase/melt partition coefficients of Sr^{2+} and Eu^{2+} arise from very close ionic radii. NWA 7325/8486 formed within an $f\text{O}_2$ of $\text{IW}-3.2 \pm 0.2$, which is more reduced than for lunar rocks that formed in a range of IW-2 to IW (Wadhwa, 2008; Sutton *et al.*, 2017). Despite their higher $f\text{O}_2$, lunar anorthosite plagioclases show similar Eu anomalies to reduced meteorites (Fig. S-4). Thus, even considering variations due to parental melt composition, there should be little difference between NWA 8486 and lunar anorthosite plagioclase compositions if they were formed under similar conditions. Although positive Eu and Sr anomalies are common in plagioclase, the present data are the first report of positive Eu and Sr anomalies in clinopyroxene in an achondritic meteorite. Europium partitioning in clinopyroxene changes depending on the composition of the system with Eu^{2+} being either similarly or less compatible than Eu^{3+} (Karner *et al.*, 2010). Therefore, the peculiar trace element inventory of NWA 8486 cannot be solely attributed to redox conditions.

Anorthosites as Source Rocks of NWA 7325/8486

NWA 8486 stands out as a unique meteorite when compared to the composition of other achondrites and lunar anorthosites. Pyroxene, plagioclase and whole rock data from all known types of achondrites define separate fields in an $\text{Eu}_\text{N}/\text{Sm}_\text{N}$ versus $\text{Sr}_\text{N}/\text{Nd}_\text{N}$ diagram (with N indicating concentrations normalised to corresponding CI chondrite abundances) (Fig. 2). The composition for NWA 8486 is shifted towards both higher $\text{Eu}_\text{N}/\text{Sm}_\text{N}$ and $\text{Sr}_\text{N}/\text{Nd}_\text{N}$ ratios compared to other planetary compositions. The rare felsic (Si-rich, evolved) achondrites GRA 06128/9 and Almahata Sitta (ALM-A clast) do not appear any different from other achondrites in terms of Eu and Sr

enrichments. Early occurrences of such felsic rocks have been related to partial melting of chondritic material instead of the multi-stage processes involved to form felsic crust on Earth (Day *et al.*, 2009; Bischoff *et al.*, 2014). Therefore, the particular composition of NWA 7325/8486 must be related to the melting of a specific source which was already enriched in Eu (relative to other REEs) and Sr. Barrat *et al.* (2015) suggested that impact melting of a gabbroic crust might produce such anomalies. In view of a homogeneous distribution of ^{26}Al in the solar system, Barrat *et al.* (2015) and Koefoed *et al.* (2016) calculated that the differentiation event for NWA 7325's parent body was ~1-2 Myr after formation of the solar system, while its crystallisation (from Pb-Pb chronometry) occurred within about 3 Myr after that. Considering the diopside-anorthite binary system at 1 atm (Osborn, 1942), the source of NWA 7325/8486 parent melt needs to be already enriched in plagioclase to reach the high plagioclase modal compositions for the meteorite, at least 48 % plagioclase to match NWA 8486. The modal composition of NWA 8486 lies on the eutectic point of the diagram. Thus, basaltic sources with low plagioclase content can produce eutectic compositions, but higher anorthite modes cannot be reached. We performed melting models of varied compositions and compared the compositions of these liquids with those in equilibrium with NWA 8486 minerals (Supplementary Information). The enrichment in Eu and the general depletion of incompatible elements are not reproduced with cumulate eucrite (Moore County) compositions (Fig. 3). The only possibility found to produce a parental magma enriched in both Eu and Sr is melting of a plagioclase-, Mg- and Ca-rich rock. Low degree melting (below 5 %) of an anorthosite (98 % anorthite) produces liquids corresponding to NWA 7325/8486 modes, but does not yield both high enough Eu anomalies and REE depletion. However, a higher pyroxene content can produce a larger amount of melt of eutectic composition. NWA 8486 features can be reproduced by 20-50 % melting of a pyroxene-rich anorthosite (Apollo noritic anorthosite 62236 with 20 % pyroxene) (Fig. 3). Anorthosites are therefore the most likely source for the parental magma of the NWA 7325/8486 suite.



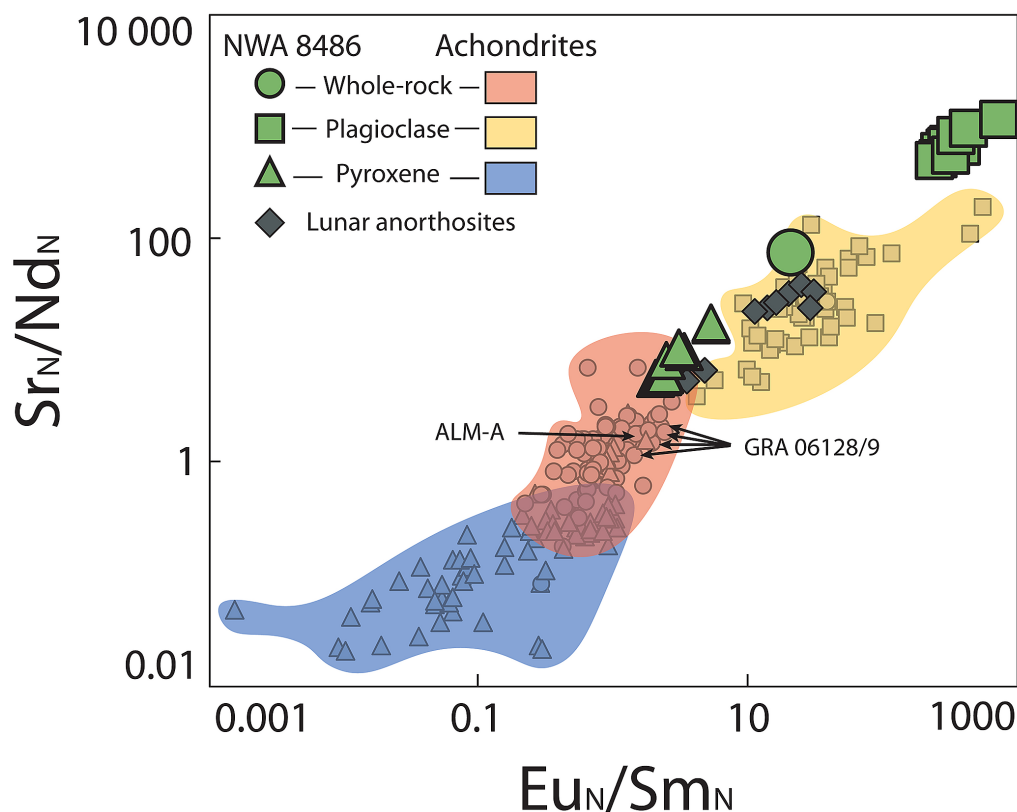


Figure 2 Eu/Sm and Sr/Nd ratios of achondrites and NWA 8486 normalised to CI chondrites (Anders and Grevesse, 1989). Overlap between the different fields is due to whole rocks mainly composed of pyroxene or plagioclase (e.g., aubrites, ureilites, lunar anorthosites). For each field group, NWA 8486 exhibits higher $\text{Eu}_\text{N}/\text{Sm}_\text{N}$ and $\text{Sr}_\text{N}/\text{Nd}_\text{N}$. Only lunar anorthosites are similar to NWA 8486 whole rock, but they contain much more plagioclase than NWA 8486. See Supplementary Information for data sources.

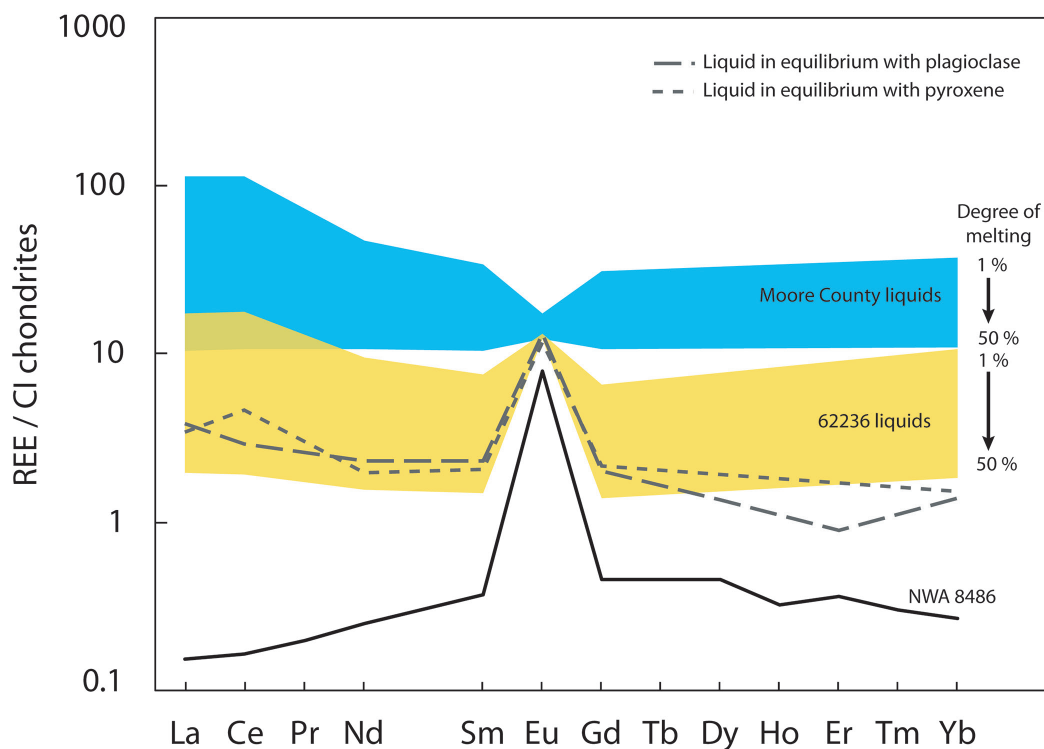


Figure 3 REE composition of liquids in equilibrium with NWA 8486 minerals (in grey dashed lines) compared to liquids modelled with compositions of the cumulate eucrite Moore County and the pyroxene-rich lunar anorthosite Apollo 62236, normalised to CI chondrites (Anders and Grevesse, 1989). A non-modal melting is considered, in agreement with petrological constraints, of eutectic proportions of 42 % plagioclase and 58 % pyroxene (Osborn, 1942). The range of composition of the liquids from 1 % to 50 % degree of melting is represented for each source composition. NWA 8486 whole rock composition is shown (black line) for comparison. See Supplementary Information for details on the model.

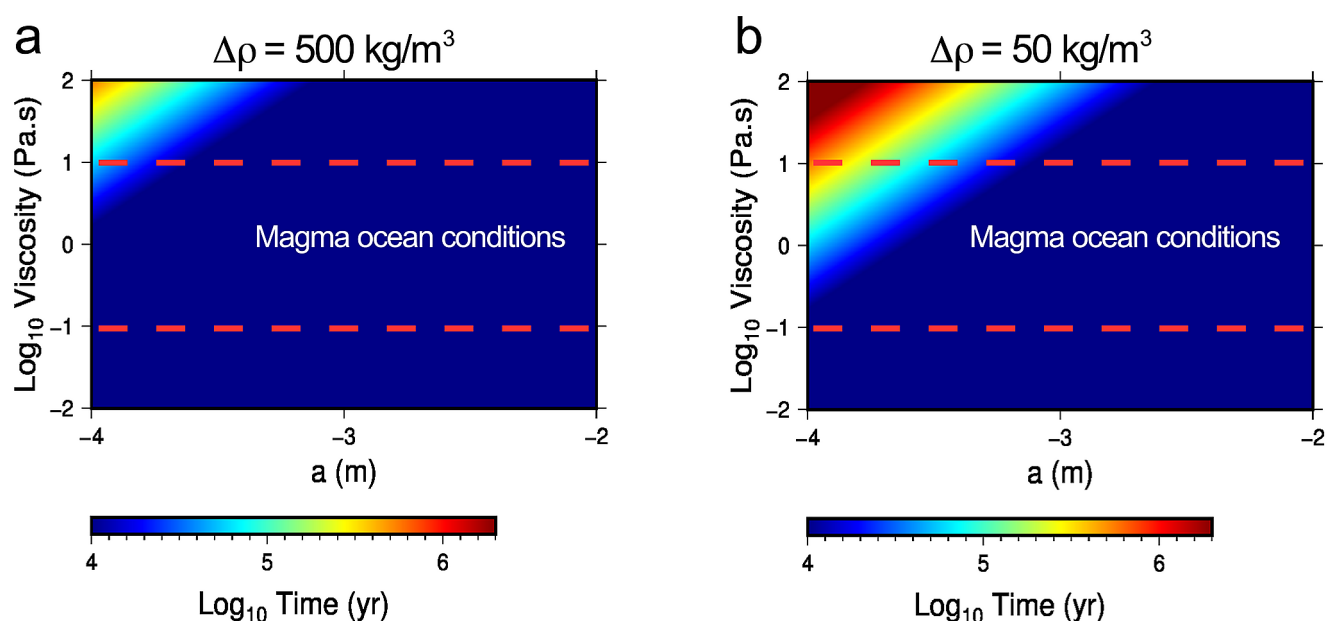


Figure 4 Time for plagioclase crystal ascent during the late stage of a magma ocean. This time is calculated for a range of viscosities (0.1 to 10 Pa.s), crystal diameters (a ; 100 μm to 1 cm) and density contrasts ($\Delta\rho$; 50 to 500 kg/m^3) between the crystal and the liquid phase. The time for a crystal to reach the surface of the magma ocean is represented with a colour scale ranging between 10 kyr (blue) and 2 Myr (red). Both panels show that the time of ascent of the crystal is a few tens of thousands of years in magma ocean conditions, except for small crystals around 100 μm and high viscosities of >10 Pa.s for which time of ascent is longer.

Timescales of Anorthosite Formation on Early Solar System Planetesimals

Anorthosites are associated with large magma systems that experience fractional crystallisation, in which plagioclase floats at the surface. Lunar anorthosites are derived from a magma ocean (MO) that formed subsequently to the Moon-forming impact event, but their petrogenesis model is still debated. Specific conditions are required for anorthositic crust formation (Albarède and Blichert-Toft, 2007). The body needs to be rather dry, as plagioclase formation is delayed in presence of water and would appear late in the crystallisation sequence (Elkins-Tanton, 2008). The size of the planetary body is also important as plagioclase is stable up to 1 GPa, which corresponds to a depth of 75 km for a Mars-like body or 200 km for a Moon-like body (Albarède and Blichert-Toft, 2007). Studies on Mercury's MO have shown that in very reduced conditions anorthite is denser than the melt and then may not float (Brown and Elkins-Tanton, 2009; Vander Kaaden and McCubbin, 2015). Crystal settling that enables anorthositic crust formation may be hindered by highly turbulent convection on small parent bodies with low gravity. Nonetheless, some authors have suggested that crystal settling can occur in such environments (Taylor *et al.*, 1993; Elkins-Tanton, 2012).

Geochemical modelling indicates that the NWA 7325/8486 source was most likely an anorthosite. Although Mercury may not be an analogue to NWA 7325/8486 parent body, it may represent an end member in terms of density and composition of the MO. Calculations have been carried out to constrain the timescales of formation of an anorthositic crust in a MO. The plagioclase formation occurs generally when the MO is crystallised by 70–80 vol. % (Supplementary Information). Assuming that the remaining molten material (≈ 20 vol. %) forms a buoyant layer over the solidified mantle and that 15 vol. % of the inner body is made of a metallic core, we can estimate the depth of the molten layer relative to the radius of the body (Supplementary Information). Considering that the rising velocity for plagioclase crystals in a MO

scales with a Stokes' Law settling velocity (Martin and Nokes, 1989), the time for a plagioclase crystal to reach the surface in a shallow MO can be assessed. The calculation yields that for the MO viscosity range (10^{-1} – 10^1 Pa.s, Dygert *et al.*, 2017) and density contrasts between crystal and magma (50–500 kg/m^3 , Brown and Elkins-Tanton, 2009; Dygert *et al.*, 2017), a crystal of at least 100 μm in diameter will reach the surface of the MO in a few tens of thousands of years (Fig. 4). The time of ascent of plagioclase is much smaller than the age of the first differentiation on NWA 7325/8486 estimated at 1.7 Ma using the ^{26}Al – ^{26}Mg systematics (Koefoed *et al.*, 2016). Therefore, we believe that NWA 7325/8486 is the first evidence of the formation and re-processing of an anorthositic crust on a planetesimal very early in the solar system.

If anorthosite could form quickly on planetesimals and magma oceans were common in the first few million years of the solar system, where are the anorthosites in the meteorite record? The reason for the absence of anorthositic crusts on achondrite parent bodies probably lies in their thermal and chemical evolution. The conditions necessary for magma oceans to form with anorthositic crusts may have been limited by the time and place of accretion (Greenwood *et al.*, 2012). Inner solar system planetesimals that accreted early were enriched in ^{26}Al and were thus more likely to have experienced magma ocean conditions (Grimm and McSween Jr, 1993). Iron meteorites are evidence of these processes. Their parent bodies were rather small (20 to 200 km; Chabot and Haack, 2006) and possibly formed within the terrestrial accretion zone below 1 AU before being scattered into the main asteroid belt. Silicate layers from these bodies have a low probability of survival in the chaotic early inner solar system (Bottke *et al.*, 2006; O'Neill and Palme, 2008). It is likely, then, that anorthositic crusts were formed in the inner solar system but rarely preserved. Material from these planetesimal silicate layers could have been subsequently added to the accreting terrestrial planets, providing a non-chondritic source for refractory lithophile elements.

Acknowledgements

We thank Dr. L. Garvie (Center for Meteorite Studies, Arizona State University) for the loan of NWA 8486, J.-L. Devidal for assistance with electron microprobe and LA-ICP-MS analyses, and J.-M. Hénot for assistance with SEM analyses. We also thank T. Withers for comments and J.-A. Barrat for enriching discussions on geochemical modelling. Helen Williams is acknowledged for editorial handling and Addi Bischoff and Stephen Elardo for constructive and thorough reviews that greatly improved the manuscript. This project has received funding from the European Research Council (ERC) under the European Union's Horizon 2020 research and innovation program (Grant Agreement No 682778 – ISOREE to MB), and NSERC Discovery Grant, Canada Research Chair, and the Canada Foundation for Innovation JELF programs (to AB). This is Laboratory of Excellence ClerVolc contribution number 369.

Editor: Helen Williams

Additional Information

Supplementary Information accompanies this letter at <http://www.geochemicalperspectivesletters.org/article1921>.



This work is distributed under the Creative Commons Attribution Non-Commercial No-Derivatives 4.0 License, which permits unre-

stricted distribution provided the original author and source are credited. The material may not be adapted (remixed, transformed or built upon) or used for commercial purposes without written permission from the author. Additional information is available at <http://www.geochemicalperspectivesletters.org/copyright-and-permissions>.

Cite this letter as: Frossard, P., Boyet, M., Bouvier, A., Hammouda, T., Monteux, J. (2019) Evidence for anorthositic crust formed on an inner solar system planetesimal. *Geochem. Persp. Let.* 11, 28–32.

References

- ALBARÈDE, F., Blichert-Toft, J. (2007) The split fate of the early Earth, Mars, Venus, and Moon. *Comptes Rendus Geosciences* 339, 917–927.
- ANDERS, E., GREVESSE, N. (1989) Abundances of the elements: Meteoritic and solar. *Geochimica et Cosmochimica Acta* 53, 197–214.
- BARRAT, J.-A., GREENWOOD, R.C., VERCHOVSKY, A.B., GILLET, P., BOLLINGER, C., LANGLADE, J.A., LIORZOU, C., FRANCHI, I.A. (2015) Crustal differentiation in the early solar system: Clues from the unique achondrite Northwest Africa 7325 (NWA 7325). *Geochimica et Cosmochimica Acta* 168, 280–292.
- BISCHOFF, A., HORSTMANN, M., BARRAT, J.-A., CHAUSSIDON, M., PACK, A., HERWARTZ, D., WARD, D., VOLLMER, C., DECKER, S. (2014) Trachyandesitic volcanism in the early solar system. *Proceedings of the National Academy of Sciences* 111, 12689–12692.
- BOTTKE, W.F., NESVORNÝ, D., GRIMM, R.E., MORBIDELLI, A., O'BRIEN, D.P. (2006) Iron meteorites as remnants of planetesimals formed in the terrestrial planet region. *Nature* 439, 821–824.
- BROWN, S.M., ELKINS-TANTON, L.T. (2009) Compositions of Mercury's earliest crust from magma ocean models. *Earth and Planetary Science Letters* 286, 446–455.
- CHABOT, N., HAACK, H. (2006) Evolution of Asteroidal Cores. In: Lauretta, D.S., McSween Jr., H.Y. (Eds.) *Meteoritics and the Early Solar System II*. The University of Arizona Press, Tucson, 747–771.
- DAY, J.M., ASH, R.D., LIU, Y., BELLUCCI, J.J., RUMBLE III, D., McDONOUGH, W.F., WALKER, R.J., TAYLOR, L.A. (2009) Early formation of evolved asteroidal crust. *Nature* 457, 179–182.

- DYGERT, N., LIN, J., MARSHALL, E.W., KONO, Y., GARDNER, J.E. (2017) A low viscosity lunar magma ocean forms a stratified anorthitic flotation crust with mafic poor and rich units. *Geophysical Research Letters* 44, 11,282–11,291.
- ELKINS-TANTON, L.T. (2008) Linked magma ocean solidification and atmospheric growth for Earth and Mars. *Earth and Planetary Science Letters* 271, 181–191.
- ELKINS-TANTON, L.T. (2012) Magma oceans in the inner solar system. *Annual Review of Earth and Planetary Science* 40, 113–139.
- GOODRICH, C.A., KITA, N.T., YIN, Q.-Z., SANBORN, M.E., WILLIAMS, C.D., NAKASHIMA, D., LANE, M.D., BOYLE, S. (2017) Petrogenesis and Provenance of Ungrouped Achondrite Northwest Africa 7325 from Petrology, Trace Elements, Oxygen, Chromium and Titanium Isotopes, and Mid-IR Spectroscopy. *Geochimica et Cosmochimica Acta* 203, 381–403.
- GREENWOOD, R., FRANCHI, I., GIBSON, J., BENEDIX, G. (2012) Oxygen isotope variation in primitive achondrites: The influence of primordial, asteroidal and terrestrial processes. *Geochimica et Cosmochimica Acta* 94, 146–163.
- GRIMM, R.E., MCSWEEN JR, H.Y. (1993) Heliocentric zoning of the asteroid belt by aluminum-26 heating. *Science* 263, 653–655.
- HASKIN, L. A., HELMKE P. A., BLANCHARD D. P., JACOBS J. W., TELANDER K. (1973) Major and trace elements abundances in samples from lunar highlands. *Proceedings of the Lunar Science Conference* 4, 1275–1296.
- KARNER, J.M., PAPIKE, J.J., SUTTON, S.R., BURGER, P.V., SHEARER, C.K., LE, L., NEWVILLE, M., CHOI, Y. (2010) Partitioning of Eu between augite and a highly spiked martian basalt composition as a function of oxygen fugacity (IW-1 to QFM): Determination of $\text{Eu}^{2+}/\text{Eu}^{3+}$ ratios by XANES. *American Mineralogist* 95, 410–413.
- KOEFOED, P., AMELIN, Y., YIN, Q.-Z., WIMPENNY, J., SANBORN, M.E., IIZUKA, T., IRVING, A.J. (2016) U–Pb and Al–Mg systematics of the ungrouped achondrite Northwest Africa 7325. *Geochimica et Cosmochimica Acta* 183, 31–45.
- LEE, T., PAPANASTASSIOU, D., WASSERBURG, G. (1977) Aluminum-26 in the early solar system-Fossil or fuel. *Astrophysical Journal* 211, L107–L110.
- MARTIN, D., NOKES, R. (1989) A fluid-dynamical study of crystal settling in convecting magmas. *Journal of Petrology* 30, 1471–1500.
- NORMAN, M.D., BORG, L.E., NYQUIST, L.E., BOGARD, D.D. (2003) Chronology, geochemistry, and petrology of a ferroan noritic anorthositic clast from Descartes breccia 67215: Clues to the age, origin, structure, and impact history of the lunar crust. *Meteoritics and Planetary Science* 38, 645–661.
- O'NEILL, H.S.C., PALME, H. (2008) Collisional erosion and the non-chondritic composition of the terrestrial planets. *Philosophical Transactions of the Royal Society A: Mathematical, Physical and Engineering Sciences* 366, 4205–4238.
- OSBORN, E.F. (1942) The system CaSiO_3 -diopside-anorthite. *American Journal of Science* 240, 751–788.
- RUZICKA, A., GROSSMAN, J., BOUVIER, A., AGEE, C.B. (2017) The Meteoritical Bulletin, No. 103. *Meteoritics and Planetary Science* 52, 1014.
- SUTTON, S.R., GOODRICH, C.A., WIRICK, S. (2017) Titanium, Vanadium and Chromium Valences in Silicates of Ungrouped Achondrite (NWA) 7325 and Ureilite Y-791538 Record Highly-Reduced Origins. *Geochimica et Cosmochimica Acta* 204, 313–330.
- TAYLOR, G.J., KEIL, K., MCCOY, T., HAACK, H., SCOTT, E.R. (1993) Asteroid differentiation: Pyroclastic volcanism to magma oceans. *Meteoritics* 28, 34–52.
- VANDER KAADEN, K.E., MCCUBBIN, F.M. (2015) Exotic crust formation on Mercury: Consequences of a shallow, FeO-poor mantle. *Journal of Geophysical Research: Planets* 120, 195–209.
- WADHWA, M. (2008) Redox conditions on small bodies, the Moon and Mars. *Reviews in Mineralogy and Geochemistry* 68, 493–510.
- WEBER, I., MORLOK, A., BISCHOFF, A., HIESINGER, H., WARD, D., JOY, K., CROWTHER, S., JASTRZEBSKI, N., GILMOUR, J., CLAY, P. (2016) Cosmochemical and spectroscopic properties of Northwest Africa 7325—A consortium study. *Meteoritics and Planetary Science* 51, 3–30.
- WOOD, J.A., DICKEY JR, J., MARVIN, U.B., POWELL, B. (1970) Lunar anorthositic and a geophysical model of the moon. *Geochimica et Cosmochimica Acta Supplements* 1, 965–988.
- YANG, J., ZHANG, C., MIYAHARA, M., TANG, X., GU, L., LIN, Y. (2019) Evidence for early impact on hot differentiated planetesimal from Al-rich micro-inclusions in ungrouped achondrite Northwest Africa 7325. *Geochimica et Cosmochimica Acta* 258, 310–335.



■ Evidence for anorthositic crust formed on an inner solar system planetesimal

P. Frossard, M. Boyet, A. Bouvier, T. Hammouda, J. Monteux

■ Supplementary Information

The Supplementary Information includes:

- 1. Methods
- 2. *In Situ* Mineral Composition
- 3. Whole-Rock and Mineral Separates Composition
- 4. Trace Element Modelling
- 5. Timescales of Plagioclase Crystals Settling
- Tables S-1 to S-11
- Figures S-1 to S-8
- Supplementary Information References

1. Methods

1.1. Scanning Electron Microprobe and Electron Microprobe Analyses

A 2.19 g chip without fusion crust and a polished mount of NWA 8486 (ASU number 1856_A_1) were obtained from the Center for Meteorite Studies at Arizona State University, USA. The one-inch epoxy polished mount was analysed with a scanning electron microprobe 5910LV JEOL at Laboratoire Magmas et Volcans (LMV) (Fig. S-1). *In-situ* geochemical analyses were carried out using an electron microprobe Cameca SX100 at LMV. Major element data and compositions were obtained on olivine (16 individual analyses), clinopyroxene (21), plagioclase (21), sulphides (26) and metal (7) (Table S-1).

1.2. Laser Ablation Inductively Coupled Spectrometry

Minerals were ablated using a 193 nm (ArF) excimer laser produced by a Resonetics M-50E system coupled with a Thermo Element magnetic sector inductively coupled plasma mass spectrometer (ICP-MS) under Ar flux. Measurements were carried out in sequences for each mineral phase. In each sequence, calibration was obtained using the NIST 612 synthetic glass standard. The quality of our measurements was assessed using a glass produced by fusion of a BCR-2 rock standard (BCR-2G). The elements analysed are Li, Mg, Si, Ca, Ti, V, Fe, Zr, Nb, REE, Hf and Ta. Electron microprobe data were used to calibrate internally the measurements for NWA 8486. Thus, plagioclase and pyroxene data were calibrated using CaO and olivine with SiO₂ abundances. The size and frequency of the



laser beam were 107 μm and 10 Hz for plagioclase and clinopyroxene, and 133 μm and 10 Hz for olivine, respectively. A second session of measurements was carried out on plagioclase and pyroxene adding Sr and Ba using the same analytical set up.

BCR-2 standard compositions were also measured as unknown samples, with a variation from reference values of 5 to 15 % for Ti, V, Sr, Zr, Nb, Ba, Rare Earth Elements (REE), and Ta. The deviation from the reported concentration for Hf was 10 to 20 % higher (see Table S-11).

1.3. Mineral Separation

The NWA 8486 chip was a thick slab without fusion crust weighing 2.19 g. The sample presented some weathering caliche at the grain boundaries several millimetres into the sample slab. NWA 8486 was therefore very slightly crushed using an agate mortar and pestle into large chunks and washed using distilled water within a Teflon beaker placed within an ultrasonic bath. The less altered material (from inspection under a binocular microscope) at the centre of the slab, weighing 1.34 g, was kept to produce a powdered whole-rock fraction and the rest processed for mineral separation. The whole-rock fraction of NWA 8486 was leached in weak hydrochloric acid (HCl) 0.4 M. The acid wash was kept for analysis.

Separation of the mineral phases was carried out in several steps in a cleanroom environment at University of Western Ontario (Western). First, crushed fragments were leached to remove caliche with nitric acid (HNO_3) 0.3 M and placed in an ultrasonic bath for 15 minutes and then 1 M HNO_3 for 90 minutes until no carbonate could be observed under the binocular microscope. Second, the fractions were separated using heavy liquids and hand-picking. The fraction for mineral separation was slightly crushed to avoid dust production and sample loss, and then sieved to retain only monocrystalline fragments between 425 μm and 100 μm in size. Clinopyroxene and plagioclase were separated using heavy liquids, namely methylene iodide (3.34 g/cm^3) and bromoform (2.9 g/cm^3) using an acid-washed Savillex Teflon filtering kit. New methylene iodide (Geoliquids) and distilled acetone were mixed to obtain a density of 3.09 g/cm^3 to efficiently separate mineral phases. Mineral fractions were further sorted by hand picking using stainless steel tweezers to obtain 314 mg of clinopyroxene and 231 mg of plagioclase. Another fraction, that consisted of composite grains with both plagioclase and clinopyroxene was dissolved and called hereafter 'Mix'. Grains were not ground to avoid further loss of sample mass during that process.

1.4. Digestion and Solution Analysis

The whole-rock powder was dissolved and analysed following the procedure detailed in Bouvier and Boyet (2016). Briefly here, NWA 8486 was dissolved on a hot plate for 48 hours beforehand, with a mixture of concentrated HF and HNO_3 (10:1). The samples were then transferred and fully dissolved using steel-jacketed Parr vessels with HF- HNO_3 (10:1) at 150 $^\circ\text{C}$ for 6 days. Fluorides were broken down using concentrated HClO_4 at 180 $^\circ\text{C}$ and then another step in HCl at 150 $^\circ\text{C}$ for 2 days to ensure complete dissolution. Mineral separates were not processed in bombs but in PFA Savillex beakers in the same manner on hot plates at 120 $^\circ\text{C}$. An aliquot of about 1-5 % was used for trace elements analysis and the remainder was used for other work.

Trace element compositions were obtained using a Thermo iCAP quadrupole ICP-MS in collision cell mode with He flux at Western. Samples were analysed in 0.3 M HNO_3 . The internal calibration was produced using certified standard solutions of various concentrations. An In internal standard was used during acquisition. The BCR-2 rock standard was analysed as unknown to control the precision and accuracy of our analyses. BCR-2 composition in Ba, Cs and REE deviate by no more than 5 % from the reference values, 10 % for transition metals, W, Th and U (Table S-3).

2. In-situ Mineral Composition

2.1. Major Elements

The mineral compositions obtained for NWA 8486 are consistent with data published by Barrat *et al.* (2015), Goodrich *et al.* (2017) and Weber *et al.* (2016) for NWA 7325. The mount of NWA 8486 studied here was poorer in olivine compared to that of Barrat *et al.* (2015) and Goodrich *et al.* (2017) but has a similar content to that of Weber *et al.* (2016) (Fig. S-1). The sample is coarse-grained, therefore, a large section or mass is required to representatively characterise it.

We observed a chemical reaction texture of plagioclase and pyroxene (Fig. S-2). The plagioclase possibly melted and dissolved pyroxene at the grain boundary and pyroxene inclusions crystallised with plagioclase subsequently. The same feature has been described and studied in detail by Goodrich *et al.* (2017) and Yang *et al.* (2019).



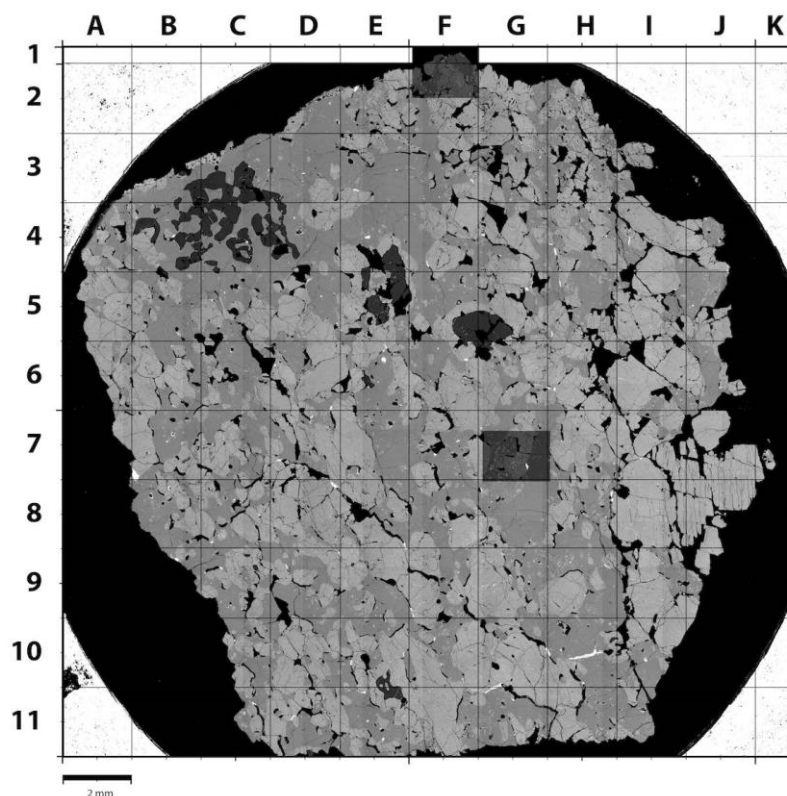


Figure S-1 Back-scattered electron composite image of the one-inch mount of NWA 8486 acquired with a Scanning Electron Microprobe (SEM). Two images were not recorded during analysis and were acquired separately, resulting in a different contrast. One can identify phases in order of brightness: clinopyroxene, plagioclase and olivine.

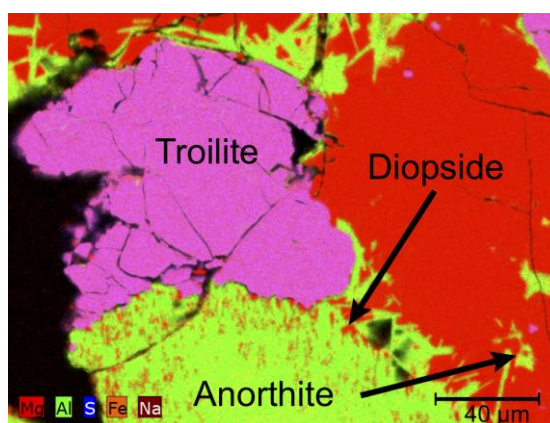


Figure S-2 Mg, Al, S, Fe and Na X-ray map taken using a SEM, showing a sulphide (purple), an anorthite (green) and a diopside grain (red). The contacts between silicate grains are uneven and display a reaction zone. Small specks of pyroxene are present at the boundary of the anorthite grain. Laths of anorthite crystallised at the contact of plagioclase. This texture can be explained as the melting of plagioclase that partially dissolved pyroxene and subsequent crystallisation of anorthite and pyroxene at the boundary.

Table S-1 Major and minor element compositions (in wt. %) of NWA 8486 obtained by *in situ* electron microprobe analysis. Average mineral compositions for each mineral phase (corresponding mineral individual analyses are indicated in bold in parentheses) and corresponding variations (2 SD) are given in parentheses. Mineral compositions are provided as anorthite (An) and albite (Ab) for plagioclase, wollastonite (Wo), enstatite (En) and ferrosilite (Fs) for pyroxene and forsterite (Fo) and fayalite (Fa) for olivine. These compositions are calculated from the molar concentration of each endmember.

	Plagioclase (19)	Pyroxene (21)	Olivine (16)		Sulphide (26)	Metal (7)
SiO ₂	46.5 (1.0)	54.3 (7)	42.0 (3)	Cr	3.6 (1.4)	
TiO ₂		0.08 (4)		Fe	57 (3)	89 (5)
Al ₂ O ₃	34.0 (1.2)	2.6 (4)	0.05 (4)	Mn	0.12 (6)	
Cr ₂ O ₃		1.0 (2)	0.4 (1)	Ni		7 (4)
FeO		0.77 (9)	2.9 (3)	S	37 (2)	
MnO		0.05 (4)	0.09 (3)			
MgO	0.3 (1)	19.1 (4)	54.2 (5)			
CaO	18.1 (9)	22.6 (4)	0.4 (2)			
Na ₂ O	1.3 (3)	0.18 (3)				
Total	100.1 (4)	100.6 (1.1)	100.0 (7)			
An	88.7 (3.0)					
Ab	11.2 (3.0)					
Wo		45.4 (5)				
En		53.5 (5)				
Fs		1.2 (1)				
Fo			97.1 (3)			
Fa			2.9 (3)			

Results for major and minor elements composition of feldspar, pyroxene, olivine and sulphide are given in Table S-1. Plagioclase can contain pyroxene inclusions and therefore spots for the analyses were carefully chosen. Among 21 points analysed for plagioclase, 2 were altered as indicated with more than 1 % MgO compared to the other values around 0.2 %. These spots were thus discarded.

Compositions of the minerals obtained in the present study are consistent with previous studies: olivine Fo_{97.1±0.3}, clinopyroxene Wo_{45.4±0.5}En_{53.4±0.5}Fs_{1.2±0.1}, plagioclase An_{88.7±3.0}Ab_{11.2±3.0}. Variability is observed in plagioclase composition. Goodrich *et al.* (2017) divided plagioclase into two categories, with high An and low An. Our data are generally intermediate between the high An and low An groups of Goodrich *et al.* The data reported here confirms that NWA 8486 is indeed paired with NWA 7325.

2.2. Trace Elements

Data on trace elements acquired *in situ* are reported in Tables S-2, S-6, S-7, S-8, S-9 and S-10 and Figure S-3.

In general, NWA 8486 is extremely depleted in incompatible elements. Olivine has very low concentrations in LREE, close to the detection limit (see Fig. S-3c) and seems to be affected by contamination in Eu and LREE. Clinopyroxene are much more enriched in REE than plagioclase except for Eu. REE compositions in NWA 8486 minerals range from a few ppb to tens of ppb. The plagioclase pattern shows strong positive Eu and Sr anomalies. Eu and Sr anomalies (Eu/Eu* and Sr/Sr*) are calculated with the following equation:

$$Eu/Eu^* = Eu_N / (Sm_N^{0.5} \times Gd_N^{0.5}) \quad \text{Eq. S-1}$$

$$Sr/Sr^* = Sr_N / (Pr_N^{0.5} \times Nd_N^{0.5}) \quad \text{Eq. S-2}$$

with Eu* and Sr* the expected concentration of the element determined by interpolation of the neighbouring elements concentrations, all normalised to CI chondrites (Anders and Grevesse, 1989).

Eu anomalies in plagioclase range from 250 to 450. Clinopyroxene exhibits also positive Eu and Sr anomalies. Ba content is variable (from 0.001 to 8 × CI chondrites), especially in clinopyroxene. Ba and Sr are generally associated to terrestrial weathering, but they are not correlated in the minerals analysed here. Barium contents of NWA 8486 are not in the range of that of samples affected by weathering (see Stelzner *et al.*, 1999 and Crozaz *et al.*, 2003). If the Sr anomaly was related to weathering, Ba content should be higher by a factor of 10 to 100.

High Ba concentrations are probably due to contamination from traces of caliche (Crozaz *et al.*, 2003). Eu and Sr anomalies in



clinopyroxene are not artefacts produced by contamination. We selected the cleanest spots for analysis where no plagioclase crystal was observed, which is consistent with the major and minor element compositions that do not indicate contamination or mixing. Furthermore, the same pattern is observed for the 27 (12 for Sr) different pyroxene grains that were analysed. Analyses were replicated on the same spots, and the concentrations were identical (see Fig. S-3b). Mineral trace element composition is quite homogeneous. Scatter appears to be related to the low concentrations, for example for Zr and Hf (Fig. 1). Some plagioclase grains exhibit higher Yb concentrations. This can be caused by an interference with $^{88}\text{Sr}^{84}\text{Kr}$ complex. Kr is present as an impurity in the Ar carrier gas that sometimes forms complexes with ions from the ablated material. The high concentration of Sr in NWA 8486 could cause interference with elements having very low concentrations, such as Yb.

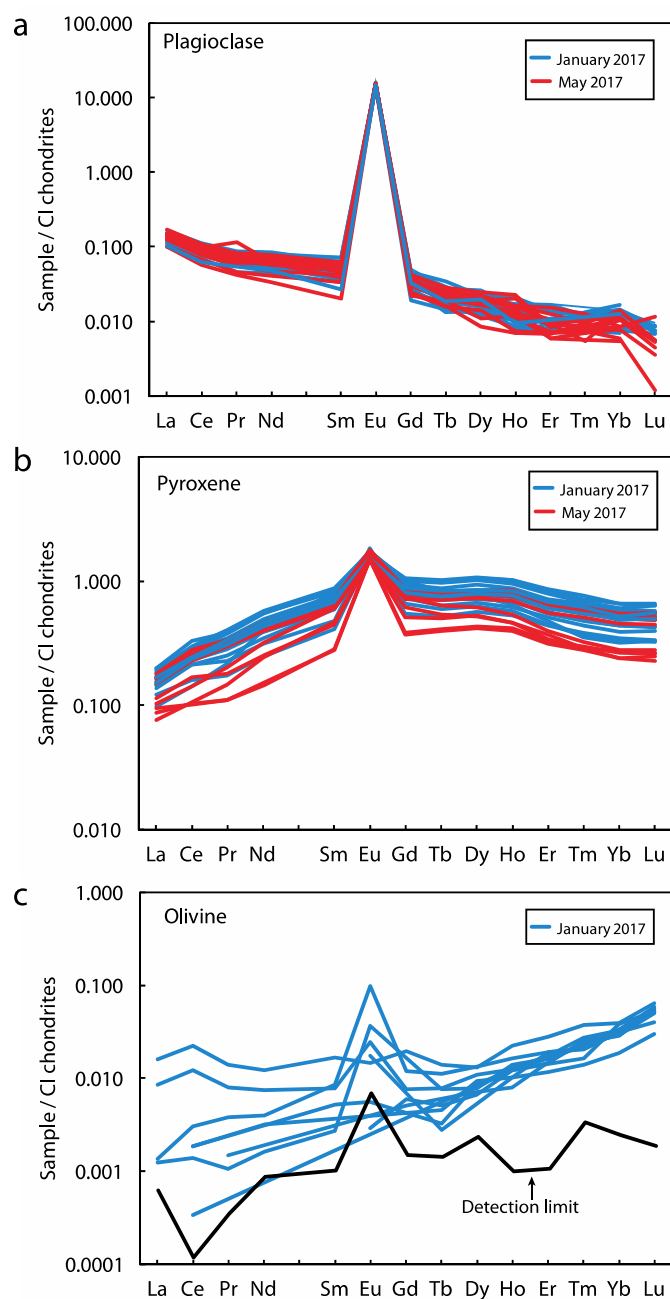


Figure S-3 REE composition normalised to CI chondrites (Anders and Grevesse, 1989) of (a) plagioclase, (b) pyroxene and (c) olivine, acquired *in situ* by LA-ICP-MS. The two sessions of measurements are represented in these graphs, January 2017 in blue and May 2017 in red. Results of the two sessions are in perfect agreement.



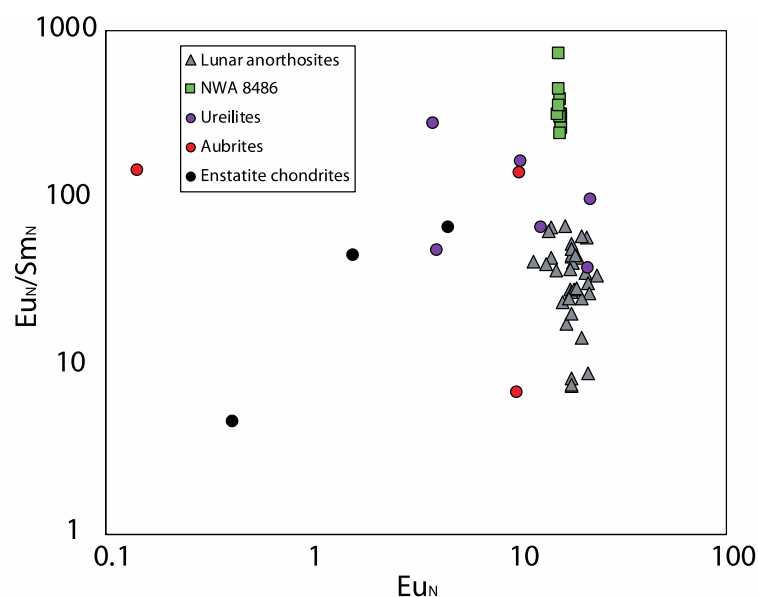


Figure S-4 Eu_N/Sm_N ratios plotted against Eu_N of plagioclases in reduced meteorites compared to NWA 8486, normalized to CI chondrites (Anders and Grevesse, 1989). High Eu_N/Sm_N ratios in enstatite chondrites, aubrites and ureilites are associated to very low concentrations in Sm. Sm measurements are close to detection limits and have thus larger errors. Eu_N/Sm_N ratios of plagioclases in lunar anorthosites are in the range of that of reduced meteorites. Data from Floss *et al.* (1998) and Papike *et al.* (1997) for lunar anorthosites, Guan and Crozaz (2001) for ureilites, Wheelock *et al.* (1994) and Hsu (1998) for aubrites and Hsu (1998) for enstatite chondrites.

3. Whole-Rock and Mineral Separates Composition

Trace elements were determined on mineral separates and whole-rock (Fig. S-5 and Table S-2). Our data on NWA 8486 is in very good agreement with the whole-rock analysis of Barrat *et al.* (2015) on NWA 7325, but is more enriched in incompatible elements. This reflects the modal composition of the split analysed, ours containing more pyroxene over plagioclase, thus likely to be more concentrated in these elements. The small Ce positive anomaly indicative of weathering in NWA 7325 is not observed in NWA 8486 due to the leaching procedure. The mild leaching process effectively removes caliche but does not alter the meteorite minerals.

NWA 8486 separates, namely plagioclase and pyroxene, are very close to the *in situ* data. The plagioclase separate contains more REE than it should, due to the presence of remaining pyroxene crystals missed during the separation process. This is particularly significant for middle-REE that exhibit the same concave pattern as clinopyroxene. Sc exhibits a positive anomaly in all the fractions, and is typically enriched in pyroxene. Whether Sc is enriched in plagioclase is difficult to assess as Sc was not analysed *in situ* and it might be related to pyroxene contamination.

The consistent Ba enrichment compared to the *in situ* compositions, especially pyroxene and whole-rock, is probably due to terrestrial carbonates. However, no Ce anomaly has been observed in the whole-rock and the mineral separates. Despite leaching the sample, terrestrial contamination is difficult to remove entirely. A significant depletion in moderately volatile elements is observed with a few ng/g of Pb, Cs, Rb and Ga.



Table S-2 Trace element concentrations for NWA 8486 in $\mu\text{g/g}$ (or ppm). Data on whole-rock, pyroxene and plagioclase separates were acquired using solution (dissolved whole-rock and mineral separates) or in situ laser (polished minerals) quadrupole inductively coupled plasma mass spectrometer (Q-ICP-MS). Trace element concentrations are reported for average composition of minerals analysed in situ with a laser ablation coupled to a mass spectrometer (LA-ICP-MS). Number of individual analysis is indicated in parentheses for each mineral, Sr and Ba were additionally analysed during a separate session with 12 individual measurements. Error on the mean is reported as 2 standard deviations (2 SD).

Concentration (ppm)	In solution (Q-ICP-MS)			In situ (LA-ICP-MS)					
	NWA 8486 whole-rock	NWA 8486 plagioclases	NWA 8486 pyroxenes	NWA 8486 plagioclase (27)	2 SD	NWA 8486 pyroxene (27)	2 SD	NWA 8486 olivine (11)	2 SD
Li				0.344	± 0.159	0.174	± 0.110	0.687	± 0.257
Sc	27.3	3.2	48.0						
Ti	361	104	468	23.4	± 6.9	493	± 204	16.3	± 4.9
V	186	26.1	334	4.45	± 0.52	365	± 86	73.5	± 4.0
Cr	3435	446	5208						
Mn	225	84.7	324						
Co	15.7	11.5	10.5						
Ni	41.2	31.4	22.1						
Cu	6.86	5.50	53.2						
Zn	3.26	2.82	30.7						
Ga	7.30	7.44	2.58						
Rb	0.063	0.101	0.079						
Sr	136	182	24.0	306	± 7	19.8	± 1.8		
Y	0.503	0.086	0.792						
Zr	0.662	0.213	1.04	0.056	± 0.178	1.11	± 1.25	0.032	± 0.014
Nb	0.031	0.029	0.051	0.002	± 0.002	0.086	± 0.022	0.030	± 0.001
Cs	0.003	0.004	0.005						
Ba	7.40	6.77	14.1	2.11	± 7.17	0.199	± 0.695		
La	0.036	0.048	0.056	0.032	± 0.009	0.036	± 0.017		
Ce	0.100	0.091	0.162	0.054	± 0.017	0.143	± 0.075		
Pr	0.018	0.011	0.027	0.006	± 0.003	0.026	± 0.015		
Nd	0.112	0.046	0.175	0.029	± 0.012	0.188	± 0.107		
Sm	0.055	0.014	0.087	0.007	± 0.004	0.097	± 0.048		
Eu	0.446	0.591	0.112	0.885	± 0.050	0.095	± 0.012	0.0003	± 0.0002
Gd	0.090	0.017	0.149	0.007	± 0.003	0.159	± 0.073	0.001	± 0.0003
Tb	0.017	0.003	0.027	0.0009	± 0.0004	0.029	± 0.013	0.0002	± 0.0001
Dy	0.110	0.018	0.180	0.005	± 0.002	0.192	± 0.086	0.002	± 0.001
Ho	0.022	0.004	0.036	0.0008	± 0.0005	0.040	± 0.019	0.0006	± 0.0002
Er	0.057	0.010	0.092	0.002	± 0.001	0.096	± 0.050	0.003	± 0.001
Tm	0.007	0.001	0.011	0.0003	± 0.0001	0.013	± 0.007	0.0006	± 0.0003
Yb	0.043	0.009	0.069	0.002	± 0.001	0.076	± 0.043	0.005	± 0.002
Lu	0.006	0.001	0.009	0.0002	± 0.0001	0.011	± 0.006	0.001	± 0.001
Hf	0.021	0.007	0.034	0.001	± 0.002	0.033	± 0.044	0.0008	± 0.001
Pb	0.014	0.044	1.683						
Th	0.006	0.011	0.019						
U	0.001	0.003	0.003						



Table S-3 Trace element composition of BCR-2 rock standard dissolved in the same procedure as NWA 8486 WR in $\mu\text{g/g}$ (or ppm). The deviation from reference values published by Jochum *et al.* (2016) are reported.

Concentration (ppm)	BCR-2	BCR-2 (Jochum <i>et al.</i> , 2016)	Deviation from reference value
Sc	30.9	33.5	8%
Ti	13061	22650	42%
V	412	418	1%
Cr	20.8	15.9	31%
Mn	1410	1523	7%
Co	36.2	37.3	3%
Ni	13.7	12.6	9%
Cu	20.8	19.7	6%
Zn	128	130	2%
Ga	21.6	22.1	2%
Rb	43.5	46.0	5%
Sr	352	337	4%
Y	33.6	36.1	7%
Zr	193	187	3%
Nb	18.1	12.4	46%
Cs	1.10	1.16	5%
Ba	661	684	3%
La	24.9	25.1	1%
Ce	52.6	53.1	1%
Pr	6.61	6.83	3%
Nd	28.7	28.3	2%
Sm	6.60	6.55	1%
Eu	2.03	1.99	2%
Gd	6.83	6.81	0.3%
Tb	1.09	1.08	1%
Dy	6.57	6.42	2%
Ho	1.34	1.31	2%
Er	3.79	3.67	3%
Tm	0.527	0.534	1%
Yb	3.47	3.39	2%
Lu	0.519	0.505	3%
Hf	5.30	4.97	7%
Pb	4.76	10.59	55%
Th	6.12	5.83	5%
U	1.72	1.68	2%

Data on plagioclase, pyroxene and whole-rock composition for $\text{Eu}_\text{N}/\text{Sm}_\text{N}$ and $\text{Sr}_\text{N}/\text{Nd}_\text{N}$ reported in Figure 3 of the main text are from the following references:

Mesosiderites: Wadhwa *et al.* (2003), Kong *et al.* (2008) and Barrat *et al.* (2015).

Eucrites: Hsu and Crozaz (1996, 1997), Barrat *et al.* (2000), Floss (2000), Yamaguchi *et al.* (2001).

Angrites: Floss *et al.* (2003).

Acapulcoites-lodranites: Floss (2000), Patzer *et al.* (2004) and Dhaliwal *et al.* (2017).

Brachinites: Swindle *et al.* (1998) and Hyde *et al.* (2014).

Shergottites, nakhlites and chassignites: Lodders (1998) and Ferdous *et al.* (2017).

Lunar anorthosites: Palme *et al.* (1984), Papike *et al.* (1997) and Norman *et al.* (2003).

Ureilites: Barrat *et al.* (2016b).

Aubrites: Barrat *et al.* (2016a).

Ungrouped achondrites: Day *et al.* (2009), Bouvier *et al.* (2011), Gardner-Vandy *et al.* (2012), Bischoff *et al.* (2014), Spivak - Birndorf *et al.* (2015), Burkhardt *et al.* (2017) and Hibiya *et al.* (2019).



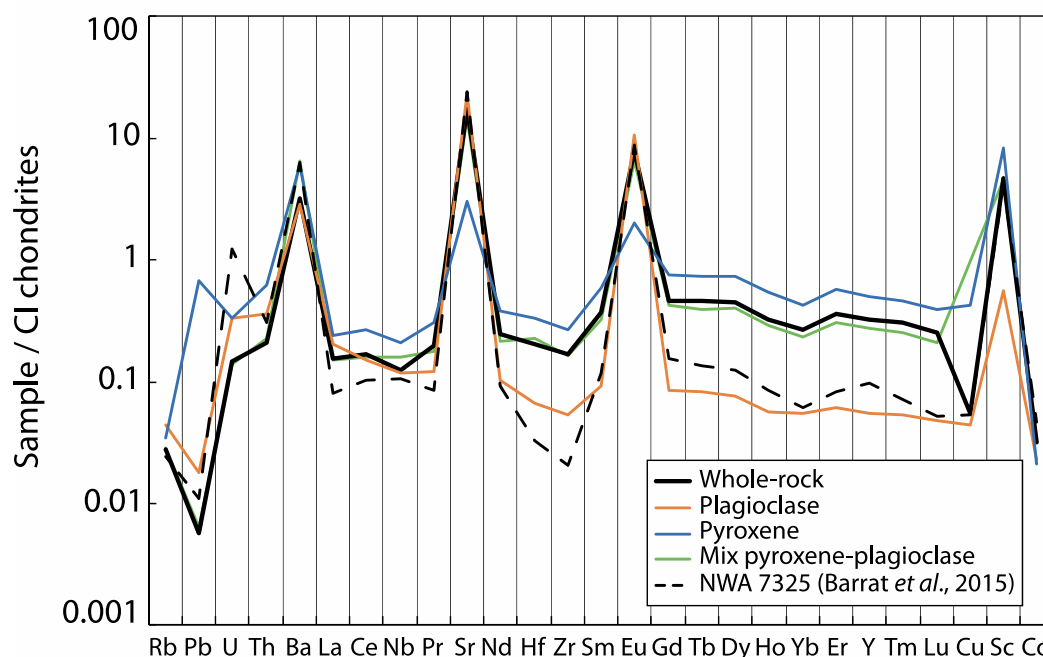


Figure S-5 Trace elements composition of whole-rock and mineral separates (plagioclase, pyroxene and ‘mix’) analysed in solution, normalised to CI chondrites (Anders and Grevesse, 1989). Elements are sorted in order of incompatibility in Earth’s continental crust (Hofmann, 1988). NWA 7325 composition from Barrat *et al.* (2015) is reported for comparison. Most of the elements are depleted compared to CI chondrites. Volatile elements (Rb and Pb) in the condensation sequence are extremely depleted. Four elements present a positive anomaly: Ba, Sr, Eu and Sc.

4. Trace Element Modelling

4.1. Model Framework

To test the plausible source rock of NWA 7325/8486, a model of melting was considered. This model calculates a REE composition of a liquid. This composition is then compared to liquids calculated in equilibrium with NWA 8486 minerals, considering they crystallised from a magma body and formed NWA 7325/8486. Petrological considerations are implemented to represent a realistic melting episode. Thus, we consider the binary eutectic phase diagram of diopside and anorthite at 1 atm (Osborn, 1942), that fits well with the mineralogy of NWA 7325/8486. Olivine is not a significant carrier of REE and will not affect the REE budget of the whole-rock.

Based on our estimates of its modal composition, NWA 8486 lies on the eutectic of this phase diagram. However, this modal composition is different from other estimates for NWA 7325. We determined the modal composition by point counting on a BSE map of the sample (Fig. S-1). The modal composition of NWA 8486 is 52 vol. % pyroxene, 44 vol. % plagioclase, 4 vol. % olivine and minor proportions of sulphides and metal. This sample is composed of millimetre-size grains and the distribution of olivine is not homogenous. The true modal composition of NWA 7325/8486 is therefore difficult to assess precisely due to its heterogeneity.

Estimates of Barrat *et al.* (2015), Weber *et al.* (2016) and Goodrich *et al.* (2017) all lie on the plagioclase side of the eutectic. Hence, it is impossible to produce such rocks from a eucritic composition of 60 vol. % pyroxene and 40 vol. % plagioclase. Addition of forsterite to the system does not change these conclusions. We choose to model the composition of NWA 8486 parental liquid as it leaves the possibility of a eucrite-type gabbro source as suggested by Barrat *et al.* (2015).

The model is calculated in one stage of non-modal melting of a source rock in eutectic proportions. The following equations are derived from Shaw (1970).

The concentration of the element i in the liquid C_i produced is calculated as such:



$$C_l^i = \frac{C_0^i}{(D_0^i + F(1 - D_{eutec}^i))} \quad \text{Eq. S-3}$$

D_0 is calculated using the modal composition of the source rock and D_{eutec} with the eutectic modal composition. F is the melting degree of the system.

The aim is not to precisely match REE compositions of NWA 8486 parental melt with that of the model, but rather to estimate the extent of the Eu enrichment and REE depletion that can be produced with different source types, as discussed below.

4.2. Parameters

Mineral/melt partition coefficients were selected from the literature to represent reduced environments (Table S-4). This consideration is important for the study of the Eu anomaly in plagioclase. Plagioclase/melt partition coefficients are from Papike *et al.* (1996) that used the data of Phinney and Morrison (1990) and Jones (1995) for Eu. These partition coefficients are suitable for lunar conditions. Clinopyroxene/melt partition coefficients are from Schosnig and Hoffer (1998), calculated from experiments in the diopside-anorthite system. These partition coefficients do not match perfectly NWA 7325/8486 conditions. We chose values that are the most suitable for our study, namely low oxygen fugacity and calcic and magnesian systems if possible. Nevertheless, the general behaviour of the elements will not differ significantly to alter Eu enrichment and other REE depletion we seek to reproduce. Europium content is dictated by plagioclase/melt partition coefficient, whereas pyroxene/melt partition coefficients control the other REE. However, the curvature of the REE pattern will not be reproduced.

Table S-4 Melt/mineral partition coefficient (D) for plagioclase and clinopyroxene used in the model. The distribution coefficient D_{eutec} is calculated from the $D_{mineral}$ and modal composition of the eutectic. Data for plagioclase is from Phinney and Morrison (1990) and Jones (1995)* for Eu and from Schosnig and Hoffer (1998) for clinopyroxene.

	$D_{\text{plagioclase}}$	$D_{\text{clinopyroxene}}$	D_{eutec}
La	0.036	0.041	0.04
Ce	0.031	0.045	0.04
Nd	0.026	0.181	0.12
Sm	0.02	0.276	0.17
Eu	1.15*	0.132	0.56
Gd	0.016	0.32	0.19
Yb	0.007	0.265	0.16

A variety of source rocks were tested to cover the possible scenario to NWA 7325/8486 formation (Table S-5). The melting model chosen is based on the anorthite-diopside phase diagram. Source rocks compositions are used as artificial compositions as there is no extraterrestrial rock fitting the constraints of the source rock of NWA 8486. Therefore, the pyroxene contents are considered as clinopyroxene for this model. A cumulate eucrite, Moore County (Barrat *et al.*, 2000) was selected, along with an ungrouped basaltic achondrite NWA 2976 (Bouvier *et al.*, 2011) to represent mafic compositions. These meteorites both exhibit a positive Eu anomaly. We chose two end-members of anorthosites in terms of pyroxene content to investigate the whole range of their composition. We selected 15415 as it is a pristine and pure anorthosite with 98 % plagioclase and 2 % diopsidic pyroxene (Hubbard *et al.*, 1971). The noritic anorthosite 62236 was chosen to represent a pyroxene-rich (about 20 %) anorthosite (Borg *et al.*, 1999; Norman *et al.*, 2003).



Table S-5 Source compositions considered for the model to reproduce the REE composition of liquids in equilibrium with NWA 8486 minerals. Data is from Barrat *et al.* (2000), Bouvier *et al.* (2011), Hubbard *et al.* (1971) and Norman *et al.* (2003) for Moore County, NWA 2976, Apollo samples 15415 and 62236 respectively.

Source	Moore County	NWA 2976	Apollo 15415	Apollo 62236
Type	Cumulate eucrite	Basaltic achondrite	Lunar anorthosite	Lunar noritic anorthosite
Plagioclase mode (wt. %)	40	43	98	80
Pyroxene mode (wt. %)	60	57	2	20
La	1.28	1.19	0.118	0.188
Ce	3.38	5.43	0.350	0.464
Pr	0.521	0.611		0.060
Nd	2.70	2.38	0.175	0.286
Sm	0.906	0.780	0.046	0.088
Eu	0.527	0.681	0.806	0.685
Gd	1.26	0.916	0.050	0.109
Tb	0.239	0.183		0.020
Dy	1.69	1.22	0.044	0.145
Ho	0.376	0.275		0.034
Er	1.10	0.867	0.019	0.106
Tm		0.118		
Yb	1.04	0.884	0.035	0.117
Lu	0.160	0.117	0.003	0.018

4.3. Models

Liquids in equilibrium with plagioclase and clinopyroxene of NWA 8486 have been calculated using the partition coefficients introduced earlier. Results are in agreement and both calculated liquids have $\text{Eu}_\text{N}/\text{Sm}_\text{N}$ ratios of 5.67 and 5.65 for plagioclase and clinopyroxene, respectively. The LREE are slightly enriched in the liquids relative to HREE. Overall, REE have compositions ranging from 1 to $5 \times \text{CI}$ chondrites.

Liquids produced by the melting model display a variety of compositions. Distribution coefficients imply that the higher the melting degree the lowest the liquid REE content. Melting in eutectic proportions yields partition coefficient D_{eutec} lower than 1, meaning that REE will preferentially incorporate the liquid rather than the solid. Europium is less incompatible than neighbouring REE ($D_{\text{eutec}} = 0.56$), as it is very strongly partitioned in plagioclase ($D_{\text{plagioclase}} = 1.15$).

The melting degree up to which liquid can be produced in eutectic proportions varies according to the modal composition of the source rocks (Fig. S-6). Pure anorthosite 15415 allows for very limited melting (3.5 %) at the eutectic, whereas 62236 allows for 34 % melting. NWA 2976 (Floss *et al.*, 2005) and Moore County (Barrat *et al.*, 2000) have a modal composition at the eutectic similarly to NWA 8486. NWA 7325 highest plagioclase mode estimates cannot be obtained with basaltic compositions, only anorthosites can produce such rocks. Considering 15415 as a source, only 5 % melting will match NWA 8486 mode, higher melting degree are unrealistic. Anorthosites with abundant pyroxene can melt to higher degree and remain in eutectic proportions.

Europium enrichment relative the other REE can be achieved only with anorthosite having already high positive Eu anomalies. However, melting degrees higher than 10 % are required. Cumulate eucrites and basaltic achondrites cannot produce this feature. Considering the depletion of REE, basaltic and eucritic compositions also fail to produce NWA 8486. High degree of melting is required to produce very low concentration even with anorthositic compositions. Indeed, REE depletion is just achieved for 20-50 % of melting with 62236 as a source. Higher degree of melting is required to explain NWA 7325 modal compositions of Barrat *et al.* (2015) and Goodrich *et al.* (2017) with 62236, reaching 50 % at maximum. Trace element modelling leads to the same conclusions in terms of the type of source as do petrological considerations within the diopside-anorthite phase diagram.



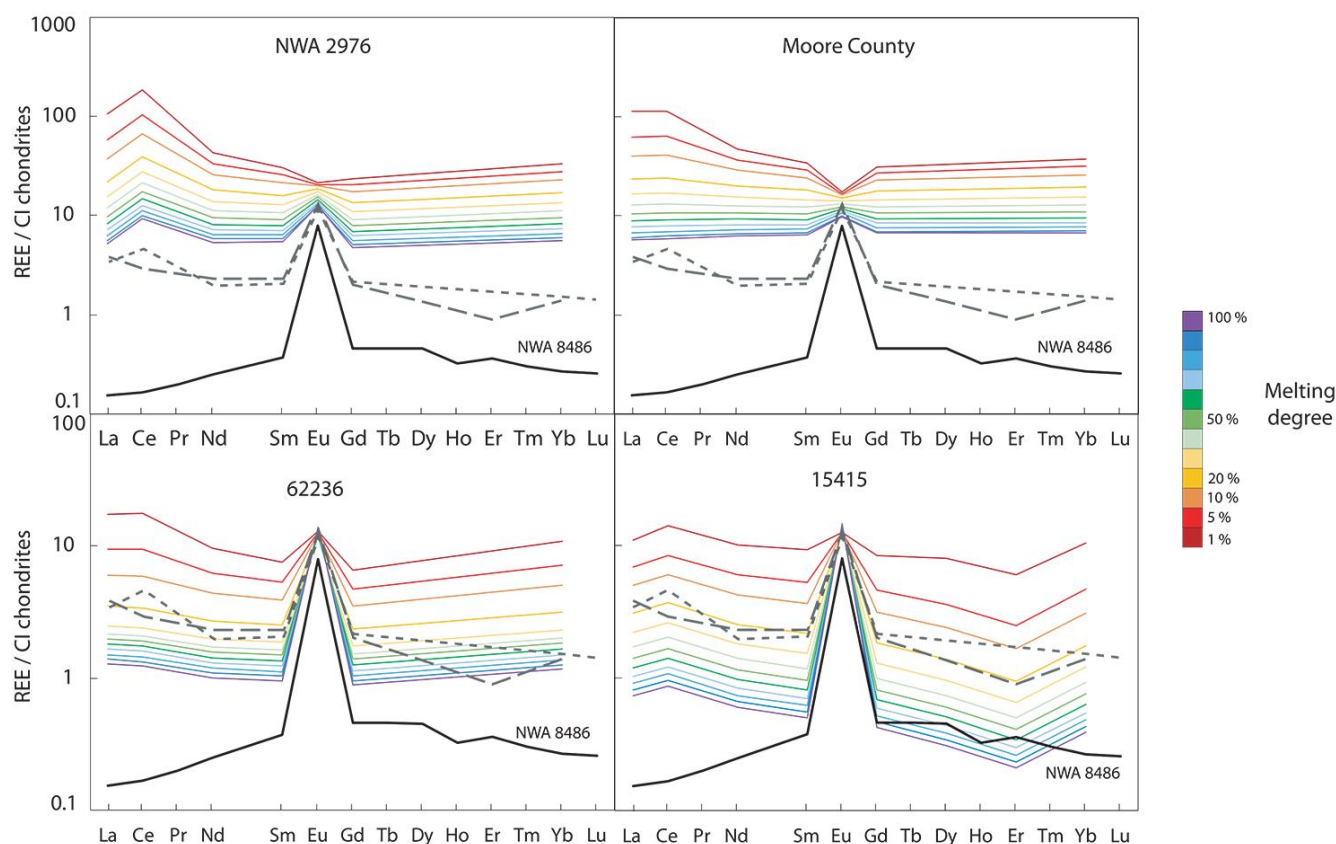


Figure S-6 REE composition of the liquids produced by the melting model for NWA 2976, Moore County, 62236 and 15415 source compositions, normalised to CI chondrites (Anders and Grevesse, 1989). For each source composition, the whole range of liquid REE composition is reported from 1 to 100% melting degree. Liquids calculated in equilibrium with the minerals are reported in grey dashed lines and NWA 8486 in black are plotted for comparison.

Interstitial melts trapped in cumulate rocks can influence significantly the composition of the whole-rock and minerals that recrystallised in equilibrium (Barrat, 2004). NWA 7325/8486 is highly depleted in incompatible elements and therefore limited amounts of interstitial melt would have been trapped as it would infer that the parental liquid was even more depleted in incompatible elements. Based on equations from Barrat (2004), apparent partition coefficients were calculated using plagioclase and clinopyroxene partition coefficients. The modal composition of the crystallising trapped melt is set to 50 % plagioclase and 50 % pyroxene as it is difficult to constrain. Liquids in equilibrium with these apparent partition coefficients and NWA 8486 minerals are reported in Figure S-7. These calculations yield that the higher the fraction of trapped melt, the higher the Eu anomaly. The degree of depletion of REE also increases with the amount of trapped melt. Comparing to the melting models of Moore County and 62236 compositions, anorthosites are the best match. However, large amounts of trapped melt imply high degrees of melting of the source rock. Therefore, trapped melt may have played a small role in NWA 7325/8486 bulk re-equilibrated composition but they most probably were not significant.



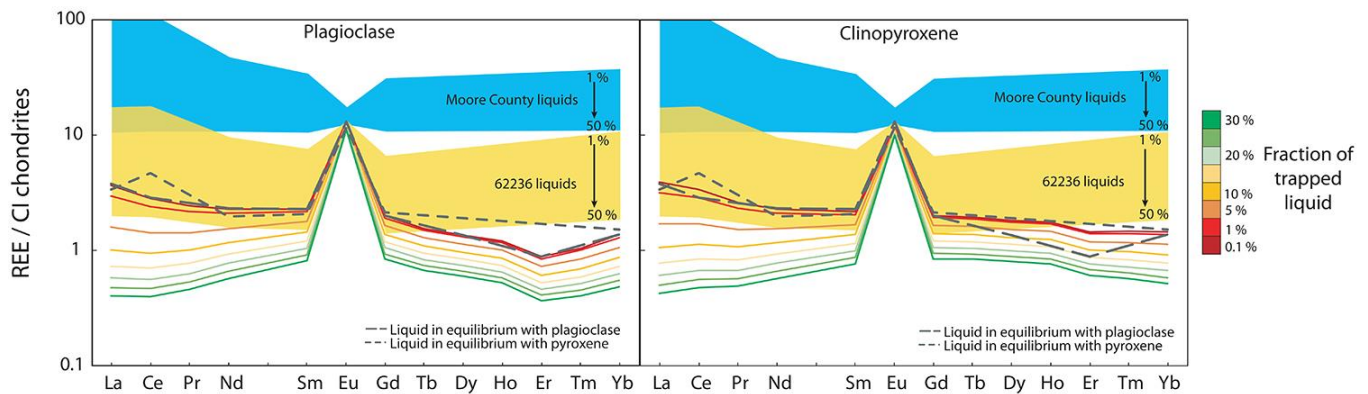


Figure S-7 Trapped melt effect on the parental liquid in equilibrium with NWA 8486 minerals. Apparent partition coefficients are calculated for several fractions of trapped melt and the corresponding liquid in equilibrium with plagioclase and clinopyroxene are reported normalised to CI chondrites (Anders and Grevesse, 1989). For comparison, liquids in equilibrium with minerals without trapped melt are reported in dashed grey lines and as well as the range of composition of modelled melts from Moore County and 62236 compositions from 1 to 50% melting degree.

5. Timescales of Plagioclase Crystals Settling

5.1. Model and Equations

Settling of crystals in a magma reservoir is possible in specific conditions. The positive contrast of density between the crystals and liquid is essential for crystals to float in a liquid reservoir. We calculated the time for a floating plagioclase crystal to reach the surface of a magma ocean in order to compare with the timescales established for NWA 7325/8486 parent body. Martin and Nokes (1989) conducted a theoretical and experimental study to characterise the settling dynamics of spherical crystals in a turbulently convecting magmatic fluid. They estimated that crystals were settling within a convective magma reservoir following a characteristic Stokes' Law settling velocity:

$$v_s = \frac{g\Delta\rho a^2}{18\eta} \quad \text{Eq. S-4}$$

where v_s is the velocity of the crystal in m/s; g is the gravity acceleration at the surface of a body (in m.s^{-2}); $\Delta\rho$ is the difference in density between the crystal and the melt (in kg/m^3); a is the diameter of the crystal (in m) and η is the fluid dynamic viscosity (in Pa.s). Plagioclase in nature are typically in tablet shapes. For simplicity, we consider here the ideal case of a spherical crystal. From this equation, we derive the time for a crystal to cover a distance z_{plg} at the velocity v_s .

Considering

$$g = \frac{4}{3}\pi G\bar{\rho}R_p \quad \text{Eq. S-5}$$

We obtain

$$t_{plg} = \frac{z_{plg}}{v_s} = \frac{18\eta z_{plg}}{\frac{4}{3}\pi G\bar{\rho}R_p\Delta\rho a^2} \quad \text{Eq. S-6}$$

where G is the gravitational constant and $\bar{\rho}$ is the mean density of the parent body with radius R_p . Using this derivation, the time t_{plg} can be compared to the chronological constraints on the formation of NWA 7325/8486.

Since we have no constraints on NWA 7325/8486 parent body in terms of size, structure and bulk composition, we consider a simple case of a body of chondritic composition with radius R_p (and volume V_p) differentiated with a metallic core and a silicate mantle (see Figure S-8). We consider that the metallic core represents $\mathcal{X}_{core} = 15$ vol. % of the body. Hence:

$$V_{core} = \mathcal{X}_{core}V_p \quad \text{Eq. S-7}$$

We also assume the end member case where the whole mantle is initially molten. Therefore, the volume of the magma ocean considered here is:

$$V_{MO} = (1 - \mathcal{X}_{core})V_p \quad \text{Eq. S-8}$$



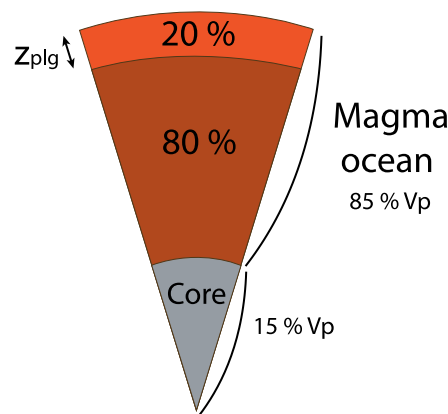


Figure S-8 Schematic representation of the inner structure of the parent body considered in our study.

To form an anorthosite crust, plagioclase has to segregate from the melt and to float toward the surface of the magma ocean. The distance that a plagioclase crystal has to travel to get to the surface is related to its nucleation site depth. The crystallisation sequence of a magma ocean is well documented for the Moon, but applications to asteroids or planetesimals are limited. Numerical modelling and high pressure and temperature studies have investigated the modal and chemical composition of the lunar magma ocean through time.

If we define \mathcal{X}_{crist} as the volume fraction of the crystallised material within the initially fully molten magma ocean, olivine generally crystallises first up to $\mathcal{X}_{crist} = 20\text{--}60\%$ (Snyder *et al.*, 1992; Elardo *et al.*, 2011; Elkins-Tanton *et al.*, 2011; Charlier *et al.*, 2018). Some authors propose that olivine crystallises along with orthopyroxene at first (Lin *et al.*, 2016). Orthopyroxene crystallises in various proportions along with olivine up to $\mathcal{X}_{crist} = 70\text{--}80\%$. These two steps are generally modelled as equilibrium crystallisation. The limit of equilibrium crystallisation is $\mathcal{X}_{crist} = 78\%$ (Elardo *et al.*, 2011). Then, a complex sequence of fractional crystallisation occurs. Clinopyroxene and plagioclase appear in the sequence at about $\mathcal{X}_{crist} = 70\text{--}80\%$. In the final stages of the ocean, Fe-Ti oxides crystallise from a magma ocean enriched in Fe, Ca and Ti. Mercury has also been investigated and may represent an endmember in terms of Mg content as it is highly reduced and in terms of internal structure with a voluminous core. The magma ocean is therefore depleted in Fe and the crystallisation sequence differs from that of the Moon (Brown and Elkins-Tanton, 2009). The numerical calculations on a modified CB chondrites (rich in metal) initial composition suggest that the sequence is somewhat similar with olivine and orthopyroxene crystallising first. Nevertheless, plagioclase crystallises when $\mathcal{X}_{crist} = 70\text{--}80\%$ in every model tested by Brown and Elkins-Tanton (2009). In our calculations, we therefore considered $\mathcal{X}_{crist} = 80\%$ as the critical value for plagioclase appearance in the crystallisation sequence.

The distance z_{plg} corresponds to the $\mathcal{X}_{plg} = 1 - \mathcal{X}_{crist} = 20\%$ remaining MO depth at the point of plagioclase appearance. The nucleation site is supposed to be distributed in the whole MO section; hence a crystal should travel the distance z_{plg} to reach the surface at maximum.

Considering that plagioclase crystallization only occurs within a volume fraction \mathcal{X}_{plg} of the MO, we get:

$$\frac{4}{3}\pi(R_p - z_{plg})^3 = (1 - \mathcal{X}_{plg})V_{MO} + V_{core} \quad \text{Eq. S-9}$$

Using $V_{MO} = (1 - \mathcal{X}_{core})V_p$ and $V_{core} = \mathcal{X}_{core}V_p$, we obtain:

$$z_{plg} = R_p \left(1 - \sqrt[3]{1 - \mathcal{X}_{plg} + \mathcal{X}_{plg}\mathcal{X}_{core}} \right) \quad \text{Eq. S-10}$$

z_{plg} expresses the distance between the nucleation site and the surface of the parent body.

From the crystal settling velocity v_s , we can now estimate the duration of the crystal settling as

$$t_{plg} = \frac{z_{plg}}{v_s} = \frac{18\eta(1 - \sqrt[3]{1 - \mathcal{X}_{plg} + \mathcal{X}_{plg}\mathcal{X}_{core}})}{\frac{4}{3}\pi G \bar{\rho} \Delta \rho a^2} \quad \text{Eq. S-11}$$



This model is therefore independent of the size of the body due to the hypothesis of a totally molten silicate mantle and the petrological constraint of the appearance of plagioclase in the crystallisation sequence. The diameter of the crystal, the molten material viscosity and the contrast of density $\Delta\rho$ will have the most significant effect on the time of settling t_{plg} .

5.2. Parameters

The contrast of density between crystals and melts varies with the Mg content of the magma and thus the degree of crystallisation of the MO. Dygert *et al.*'s (2017) study on the lunar magma ocean in its final stages during plagioclase crystallisation consider a $\Delta\rho$ of 600 to 200 kg/m³. As NWA 7325/8486 is reduced, we compare the lunar values to the Mercury endmember. Brown and Elkins-Tanton (2009) investigated the possibility of plagioclase floatation in a magma on Mercury and suggest that plagioclase has either a higher density than the liquid or a contrast of density between plagioclase and melt below 50-100 kg/m³. From density experiments in a possible Mercurian melt, Vander Kaaden and McCubbin (2015) conclude that plagioclase cannot float in Mercurian conditions. The liquid they use has the composition of a flood basalt observed on Mercury's surface, rich in SiO₂, which is different than the terminal MO compositions obtained by fractional crystallisation of Mercury's magma ocean (Brown *et al.*, 2009). Therefore, we consider NWA 7325/8486 parent body as an intermediate case of anorthositic crust formation between Mercury and the Moon. To characterise the influence of the density contrast on the settling timescale of plagioclase crystals, we consider positive $\Delta\rho$ values favouring anorthositic crust formation and ranging between 50 and 500 kg/m³.

The viscosity of the magma ocean in its final stages has also been investigated by Dygert *et al.* (2017) on the Moon. This study yields a range of 0.22 to 1.45 Pa.s, based on experiments at 0.1 to 4.4 GPa and 1300 to 1600 °C. We chose to calculate t_{plg} between 10⁻² to 10² Pa.s to cover a large range of viscosities, but MO conditions are most likely between 10⁻¹ and 10¹ Pa.s.

The diameter of plagioclase crystals is critical in terms of the dynamic, namely if the crystal settles or is entrained in the convection. Suckale *et al.* (2012) suggest that crystals can settle if they have a diameter larger than 2 mm on average. The critical diameter of a crystal to be entrained in the convective flow can be calculated. It varies with the contrast of density, gravity, and thermal parameters of the MO. Dygert *et al.* (2017) calculated the critical diameter of a plagioclase crystal throughout the evolution of the final stage of the magma ocean. They suggest that it decreases with the crystallisation of the MO, from 100 µm at the start to about 2 µm at the end. Crystals likely form and reach 100 µm in a MO, therefore, we use the range of 100 µm to 1 cm in our calculations.

Among the other parameters present in Equation S-11, we have chosen to fix the volume fraction of the core ($V_{core} = 15\% V_p$), the volume fraction of the molten zone where plagioclase crystallisation occurs ($V_{plg} = 20\% V_{MO}$), and the mean density of the parent body ($\bar{\rho} = 3300$ kg/m³). As their variability is less important (cube root) than the variability of η , $\Delta\rho$ and a , their influence on the settling time t_{plg} can be considered here as marginal.

5.3. Results

The results of our calculations in the conditions set in the previous sections are presented in Figure 4. For the range of parameters investigated, the time for a plagioclase crystal to reach the surface of the magma ocean is below 10 000 years. A lower contrast of density $\Delta\rho$ yields a longer time of ascent, but still below tens of thousands of years. At high viscosities (> 10 Pa.s) and for a crystal of about 100 µm, the time of ascent reaches a few hundred thousand years. As evidenced by Dygert *et al.* (2017), high viscosities are generally associated with a higher critical diameter of crystals. The magma gets more viscous towards the end of the crystallisation or at the surface with lower temperatures. Therefore, high viscosity and low diameter probably do not describe realistic conditions.

These results suggest that plagioclase can segregate from the magma and rise very quickly. The age of the first differentiation on NWA 7325/8486, possibly through magma ocean processes, has been estimated at about 1.7 Ma using the ²⁶Al-²⁶Mg systematics (Koefoed *et al.*, 2016). The time of ascent of plagioclase is much smaller than the age of NWA 7325/8486 source. It is therefore possible for a plagioclase crust to form in a very short period, compatible with the timescales of NWA 7325/8486 formation.



Supplementary Tables S-6 to S-11**Table S-6** Trace elements composition of NWA 8486 plagioclase acquired *in situ* by LA-ICP-MS, in µg/g (or ppm) for the first session in January 2017. Individual measurements and mean minimum detection limit reported here are calculated using the GLITTER software.

Composition (ppm)	Plg 1	Plg 2	Plg 3	Plg 4	Plg 5	Plg 6	Plg 7	Plg 8	Plg 9	Plg 10	Plg 11	Plg 12	Plg 13	Plg 14	Plg 15	Detection limit (ppm)
Li	0.213	0.241	0.255	0.308	0.21	0.237	0.258	0.287	0.305	0.277	0.302	0.291	0.261	0.269	0.286	0.021
Mg	1869	1602	1726	2767	2200	1759	1992	1956	1701	1812	1727	1692	1731	1708	1940	0.04
Si	238527	233799	232555	250117	230554	269968	216723	229797	228916	250400	259096	250584	268248	240905	239944	22
Ca	127503	128575	128289	131862	126073	133006	123072	128217	121428	133435	133435	123143	132291	126431	130647	5.8
Ti	23.3	23.6	23.4	23.8	30.9	28.4	23.9	29.1	19.7	21.9	18.3	19.7	22.9	21.4	26.5	0.16
V	5.18	4.18	4.26	4.8	4.62	4.44	4.1	4.59	4.35	4.85	4.62	4.41	4.59	4.31	4.75	0.0048
Fe	4104	232	328	1622	516	315	291	353	406	305	268	290	261	434	602	0.9
Sr																
Zr	<0.0169	<0.0117	<0.0112	<0.0120	<0.0103	<0.0113	0.0126	<0.0097	<0.0094	<0.0106	0.0105	<0.0081	<0.0105	<0.0091	0.0198	0.011
Nb	0.0047	0.0011	0.0012	0.0037	0.0021	0.0019	0.0015	0.0020	0.0015	0.0019	0.0017	0.0012	0.0019	0.0019	0.0024	0.0002
Ba																
La	0.0247	0.0271	0.0298	0.0289	0.0364	0.0351	0.0292	0.0399	0.0295	0.0360	0.02432	0.0279	0.0351	0.0313	0.0369	0.0004
Ce	0.0380	0.0476	0.0528	0.0507	0.0637	0.0564	0.0497	0.0687	0.0496	0.0505	0.0425	0.0477	0.0600	0.0527	0.0663	0.0005
Pr	0.0051	0.0054	0.007	0.0064	0.0072	0.0062	0.0055	0.0082	0.0059	0.0066	0.0043	0.0057	0.0066	0.0057	0.0075	0.0002
Nd	0.0226	0.0222	0.0281	0.0277	0.0352	0.0300	0.0261	0.0397	0.0247	0.0322	0.0208	0.0254	0.0310	0.0301	0.0374	0.0013
Sm	0.0041	0.0067	0.00816	0.0070	0.0111	0.0082	0.0077	0.0094	0.0065	0.0070	0.0051	0.0056	0.0067	0.0063	0.0109	0.0014
Eu	0.867	0.890	0.882	0.927	0.875	0.924	0.857	0.904	0.83	0.921	0.921	0.837	0.91	0.853	0.895	0.0004
Gd	0.0068	0.0053	0.0079	0.0106	0.0094	0.0058	0.0059	0.0075	0.0039	0.0056	0.0068	0.0054	0.0084	0.0078	0.0095	0.0019
Tb	0.0007	0.0006	0.00101	0.0011	0.0012	0.0009	0.0005	0.0010	0.0006	0.0011	0.0007	0.0007	0.0009	0.0007	0.0014	0.0002
Dy	0.0050	0.0036	0.00439	0.0069	0.0049	0.0050	0.0035	0.0050	0.0032	0.0052	0.0028	0.0030	0.0060	0.0041	0.0056	0.0009
Ho	0.0005	0.0008	0.00094	0.0009	0.0010	0.0004	0.0005	0.0009	0.0007	0.0008	0.0006	0.0005	0.0009	0.0005	0.0012	0.0002
Er	<0.00150	0.0018	<0.00094	0.0029	0.0027	0.0016	0.0018	0.0022	0.0018	0.0017	<0.00088	<0.00077	0.0014	0.0012	0.0023	0.0008
Tm	<0.00022	<0.00021	<0.00021	<0.00023	0.0003	0.0004	<0.00015	0.0003	0.0002	<0.00017	<0.00019	<0.00016	0.0003	0.0002	0.0003	0.0002
Yb	0.0021	<0.00103	<0.00116	0.0024	0.0022	0.0028	0.0019	0.0025	<0.00118	<0.00108	<0.00122	0.00117	0.0020	0.0018	0.0024	0.0011
Lu	<0.00026	<0.00017	<0.00016	0.0002	0.0002	<0.00017	<0.00010	0.0002	0.0002	<0.00017	0.0002	<0.00018	0.0002	0.0001	<0.00015	0.0002
Hf	<0.00135	<0.00065	<0.00079	0.0014	<0.00081	<0.00069	<0.00057	0.0006	<0.00098	<0.00126	0.0012	<0.00064	<0.00096	0.0006	<0.00060	0.0008
Ta	<0.00046	0.0004	<0.00036	<0.00041	<0.00033	<0.00039	<0.00032	<0.00034	<0.00033	0.0005	<0.00036	<0.00033	<0.00040	0.0005	<0.00036	0.0003



Table S-7 Trace elements composition of NWA 8486 plagioclase acquired *in situ* by LA-ICP-MS, in µg/g (or ppm) for the first session in May 2017. Individual measurements and mean minimum detection limit reported here are calculated using the GLITTER software.

Composition (ppm)	Plg 1	Plg 2	Plg 3	Plg 4	Plg 5	Plg 6	Plg 7	Plg 8	Plg 9	Plg 10	Plg 11	Plg 12	Detection limit (ppm)
Li	0.324	0.333	0.390	0.327	0.320	0.231	0.308	0.296	0.371	0.297	0.383	0.282	0.019
Mg	2679	3316	2721	2755	3851	2563	2886	2868	2987	2535	3322	2421	0.23
Si	225343	230793	226908	228663	230610	224628	229193	228769	230388	229754	227782	226702	37
Ca	129526	129876	129522	129623	129563	128946	129331	128917	129143	128813	127669	127991	5.0
Ti	26.0	27.0	24.9	24.3	23.9	25.2	23.7	23.8	19.7	20.9	17.8	16.8	0.13
V	4.18	4.60	4.25	4.24	4.32	4.12	4.22	4.61	4.60	4.26	4.48	4.22	0.0047
Fe	295	333	262	249	468	582	321	292	317	213	328	349	0.4
Sr	304	309	308	305	306	310	315	304	303	304	306	302	0.0018
Zr	0.302	0.0286	0.0242	0.0394	0.0087	0.0177	0.196	0.0185	<0.0052	<0.0044	0.0214	0.0238	0.004
Nb	0.0020	0.0019	0.0014	0.0013	0.0022	0.0038	0.0012	0.0023	0.0021	0.0010	0.0017	0.0015	0.0001
Ba	1.17	1.15	1.12	1.20	1.05	1.05	1.13	0.977	13.5	1.06	1.22	0.676	0.0028
La	0.0341	0.0353	0.0340	0.0322	0.0301	0.0353	0.0308	0.0406	0.0359	0.0302	0.0245	0.0238	0.0002
Ce	0.0608	0.0587	0.0558	0.0537	0.0496	0.0630	0.0527	0.0667	0.0620	0.0475	0.0420	0.0356	0.0002
Pr	0.0107	0.0068	0.0068	0.0062	0.0058	0.0071	0.0061	0.0076	0.0071	0.0052	0.0043	0.0039	0.0001
Nd	0.0291	0.0319	0.0284	0.0272	0.0275	0.0361	0.0284	0.0372	0.0334	0.0220	0.0192	0.0159	0.0005
Sm	0.0079	0.0088	0.0074	0.0073	0.0075	0.0089	0.0060	0.0094	0.0070	0.0064	0.0052	0.0031	0.0006
Eu	0.899	0.899	0.892	0.886	0.879	0.893	0.887	0.879	0.857	0.875	0.877	0.875	0.0002
Gd	0.0066	0.0078	0.0062	0.0063	0.0072	0.0087	0.0066	0.0086	0.0073	0.0045	0.0051	0.0048	0.0009
Tb	0.0008	0.0009	0.0008	0.0008	0.0009	0.0011	0.0008	0.0011	0.0010	0.0008	0.0006	0.0006	0.0001
Dy	0.0043	0.0049	0.0053	0.0042	0.0052	0.0063	0.0049	0.0049	0.0057	0.0028	0.0036	0.0022	0.0004
Ho	0.0007	0.0009	0.0008	0.0007	0.0009	0.0013	0.0006	0.0011	0.0009	0.0007	0.0004	0.0004	0.0001
Er	0.0016	0.0017	0.0010	0.0015	0.0021	0.0014	0.0012	0.0015	0.0025	0.0010	0.0012	0.0011	0.0003
Tm	0.0003	0.0002	0.0002	0.0002	0.0003	0.0003	<0.00009	0.0001	0.0003	<0.00011	0.0002	0.0003	0.0001
Yb	0.0021	0.0017	0.0013	0.0019	0.0023	0.0018	0.0014	0.0023	0.0014	0.0009	0.0010	0.0013	0.0004
Lu	<0.00009	<0.00013	0.0001	0.0001	0.0001	0.0001	<0.00014	<0.00012	0.0003	<0.00012	0.0000	<0.00006	0.0001
Hf	0.0041	0.0005	0.0005	0.0004	0.0004	<0.00028	0.0023	0.0005	<0.00078	<0.00027	0.0003	<0.00043	0.0003
Ta	<0.00018	0.0002	0.0003	<0.00019	<0.00017	<0.00015	<0.00021	<0.00019	<0.00016	0.0002	<0.00017	<0.00019	0.0002



Table S-8 Trace elements composition of NWA 8486 pyroxene acquired *in situ* by LA-ICP-MS, in µg/g (or ppm) for the first session in January 2017. Individual measurements and mean minimum detection limit reported here are calculated using the GLITTER software.

Composition (ppm)	Px 1	Px 2	Px 3	Px 4	Px 5	Px 6	Px 7	Px 8	Px 9	Px 10	Px 11	Px 12	Px 13	Px 14	Px 15	Detection limit (ppm)
Li	0.0255	0.178	0.0845	0.0976	0.0808	0.155	0.149	0.163	0.158	0.145	0.155	0.113	0.124	0.140	0.125	0.012
Mg	173488	176108	173895	173572	174274	175416	179938	176282	177121	169346	176905	174176	160484	166317	179086	0.13
Si	273695	277227	277985	279341	273388	278118	279849	272467	279708	265840	274699	266150	253712	260323	276909	11
Ca	160808	164167	163452	162523	161451	160593	163881	162523	161237	159593	163166	160736	160093	163023	162237	3.8
Ti	551	533	473	436	441	450	526	767	411	353	507	588	608	527	408	0.12
V	371	352	396	448	400	408	337	288	413	409	409	366	369	391	403	0.0034
Fe	10043	9638	10764	11157	11200	10467	9999	9713	16211	11034	11251	10195	8873	9923	10109	0.9
Sr																
Zr	1.58	1.41	1.39	1.22	1.02	1.08	0.647	0.398	0.529	0.401	1.57	1.90	2.24	2.24	1.16	0.006
Nb	0.0946	0.0919	0.0932	0.0994	0.0990	0.0988	0.0896	0.0866	0.104	0.0979	0.101	0.0924	0.0926	0.0936	0.0913	0.0002
Ba																
La	0.0402	0.0399	0.0399	0.0450	0.0357	0.0372	0.0348	0.0236	0.0329	0.0294	0.0434	0.0478	0.0480	0.0466	0.0355	0.0003
Ce	0.167	0.166	0.164	0.178	0.143	0.153	0.132	0.0883	0.131	0.0985	0.180	0.205	0.177	0.184	0.165	0.0004
Pr	0.0313	0.0313	0.0296	0.0304	0.0264	0.0269	0.0236	0.0202	0.0214	0.016	0.0327	0.036	0.0355	0.0377	0.0293	0.0001
Nd	0.226	0.217	0.218	0.199	0.185	0.191	0.165	0.192	0.149	0.116	0.235	0.263	0.259	0.273	0.201	0.0007
Sm	0.115	0.109	0.107	0.0971	0.0918	0.0943	0.0914	0.127	0.0733	0.0629	0.117	0.126	0.132	0.135	0.0952	0.0008
Eu	0.0964	0.0986	0.0992	0.0965	0.0980	0.0986	0.0966	0.1021	0.109	0.0949	0.103	0.0982	0.0984	0.101	0.0955	0.0003
Gd	0.183	0.174	0.175	0.158	0.155	0.160	0.149	0.207	0.136	0.112	0.192	0.206	0.217	0.213	0.164	0.0013
Tb	0.0326	0.0308	0.0312	0.0286	0.0283	0.0278	0.0254	0.0332	0.0236	0.0207	0.0345	0.0385	0.0405	0.0394	0.0294	0.0001
Dy	0.218	0.212	0.213	0.198	0.184	0.186	0.170	0.196	0.159	0.144	0.238	0.260	0.272	0.269	0.207	0.0005
Ho	0.0474	0.0448	0.0439	0.0415	0.0387	0.0381	0.0346	0.0367	0.0325	0.0298	0.0490	0.0534	0.0579	0.0578	0.0460	0.0001
Er	0.113	0.109	0.111	0.100	0.0908	0.0936	0.0839	0.0783	0.0744	0.0728	0.119	0.131	0.138	0.143	0.115	0.0004
Tm	0.0152	0.0151	0.0145	0.0148	0.0125	0.0126	0.0115	0.0092	0.0096	0.0100	0.0171	0.0178	0.0187	0.0199	0.0162	0.0001
Yb	0.0916	0.0873	0.0884	0.0820	0.0743	0.0742	0.0657	0.0536	0.0566	0.0589	0.101	0.101	0.111	0.110	0.0967	0.0011
Lu	0.0134	0.0127	0.0136	0.0126	0.0107	0.0106	0.0100	0.0082	0.0082	0.0084	0.0143	0.0160	0.0164	0.0160	0.0136	0.0001
Hf	0.0485	0.0378	0.0275	0.0222	0.0228	0.0248	0.0207	0.0455	0.0128	0.0065	0.0426	0.0648	0.0937	0.0562	0.0142	0.0005
Ta	0.0017	0.0016	0.0018	0.0024	0.0018	0.0020	0.0017	0.0011	0.0024	0.0021	0.0024	0.0019	0.0026	0.0022	0.0022	0.0002



Table S-9 Trace elements composition of NWA 8486 pyroxene acquired *in situ* by LA-ICP-MS, in µg/g (or ppm) for the first session in May 2017. Individual measurements and mean minimum detection limit reported here are calculated using the GLITTER software.

Composition (ppm)	Px 1	Px 2	Px 3	Px 4	Px 5	Px 6	Px 7	Px 8	Px 9	Px 10	Px 11	Px 12	Detection limit (ppm)
Li	0.179	0.194	0.186	0.183	0.165	0.223	0.219	0.204	0.204	0.186	0.182	0.189	0.009
Mg	192380	196898	192635	197186	186755	194308	190905	190328	194801	196383	193477	198718	0.12
Si	246037	251974	244952	251080	238451	247761	247242	245347	248767	249257	241246	250137	17
Ca	157912	158597	157849	158659	158042	157895	158775	159032	158232	159003	157278	158516	2.6
Ti	633	533	530	469	526	417	470	326	318	626	365	530	0.08
V	308	343	353	315	349	376	357	382	400	285	349	286	0.0024
Fe	6756	7564	7150	7444	8014	7258	7214	6831	7282	7279	7007	7986	0.3
Sr	19.9	19.5	19.8	19.3	21.4	18.9	21.7	19.9	19.3	19.9	18.6	19.5	0.0008
Zr	1.65	1.37	1.48	1.01	1.76	1.32	1.31	0.187	0.167	0.344	0.409	0.176	0.002
Nb	0.0721	0.0760	0.0760	0.0701	0.0813	0.0758	0.0780	0.0781	0.0818	0.0703	0.0784	0.0702	0.0001
Ba	0.619	0.0035	0.395	0.0057	0.0350	0.0474	1.05	<0.00099	0.0018	0.0027	0.0186	0.0073	0.0009
La	0.0402	0.0368	0.0390	0.0361	0.0410	0.0373	0.0436	0.0227	0.0209	0.0249	0.0275	0.0185	0.0002
Ce	0.152	0.146	0.155	0.142	0.157	0.152	0.173	0.0631	0.0636	0.0878	0.104	<0.005	0.0005
Pr	0.0315	0.0291	0.0305	0.0278	0.0314	0.0287	0.0315	0.0104	0.0103	0.0189	0.0170	0.0139	0.0001
Nd	0.219	0.204	0.210	0.187	0.219	0.199	0.218	0.0722	0.0680	0.1496	0.118	0.115	0.0003
Sm	0.111	0.104	0.105	0.0930	0.110	0.0997	0.107	0.0426	0.0431	0.0934	0.0687	0.0725	0.0003
Eu	0.0876	0.0890	0.0943	0.0862	0.104	0.0867	0.0997	0.0876	0.0889	0.0882	0.0893	0.0873	0.0001
Gd	0.181	0.165	0.165	0.148	0.179	0.158	0.171	0.0787	0.0767	0.152	0.105	0.127	0.0006
Tb	0.0329	0.0300	0.0301	0.0277	0.0326	0.0306	0.0313	0.0163	0.0157	0.0252	0.0198	0.0214	0.0001
Dy	0.216	0.201	0.199	0.185	0.214	0.199	0.206	0.111	0.106	0.158	0.135	0.133	0.0002
Ho	0.0468	0.0429	0.0429	0.0388	0.0476	0.0427	0.0444	0.0234	0.0223	0.0302	0.0260	0.0262	0.0001
Er	0.113	0.100	0.101	0.0922	0.109	0.101	0.103	0.0545	0.0520	0.0652	0.0612	0.0567	0.0002
Tm	0.0161	0.0142	0.0143	0.0133	0.0160	0.0156	0.0152	0.0078	0.0073	0.0085	0.0076	0.0076	0.0000
Yb	0.0869	0.0832	0.0848	0.0768	0.0922	0.0844	0.0864	0.0444	0.0404	0.0471	0.0457	0.0406	0.0004
Lu	0.0138	0.0124	0.0121	0.0113	0.0138	0.0122	0.0130	0.0065	0.0062	0.0069	0.0066	0.0057	0.0001
Hf	0.0633	0.0427	0.0454	0.0187	0.0591	0.0235	0.0338	0.0041	0.0033	0.0265	0.0083	<0.0029	0.0004
Ta	0.0015	0.0017	0.0017	0.0013	0.0018	0.0019	0.0021	0.0019	0.0021	0.0012	0.0017	0.0011	0.0001



Table S-10 Trace elements composition of NWA 8486 olivine acquired *in situ* by LA-ICP-MS, in $\mu\text{g/g}$ (or ppm) for the first session in January 2017. Individual measurements and mean minimum detection limit reported here are calculated using the GLITTER software.

Composition (ppm)	OI 1	OI 2	OI 3	OI 4	OI 5	OI 6	OI 7	OI 8	OI 9	OI 10	Detection limit (ppm)
Li	0.840	0.677	0.554	0.575	0.666	0.665	0.524	0.733	0.569	0.705	0.016
Mg											
Si	197072	197540	196184	196231	197072	197493	196184	196699	196979	195390	16
Ca	2205	2115	2433	2086	2127	2066	2108	2063	2902	2046	4.8
Ti	18.5	17.5	17.8	17.5	17.3	17.1	15.4	15.8	17.0	11.6	0.11
V	70.6	72.1	72.6	73.5	70.9	75.1	74.4	73.6	71.6	76.1	0.0037
Fe	30018	30482	30062	30479	28941	31001	31581	29756	28423	27665	0.4
Sr											
Zr	0.0355	0.0434	0.0354	0.0329	0.0428	0.0235	0.0378	0.0254	0.0052	0.0342	0.003
Nb	0.0290	0.0297	0.0298	0.0293	0.0297	0.0310	0.0308	0.0304	0.0318	0.0300	0.0001
Ba											
La	<0.00016	<0.00017	0.0003	<0.00019	0.0038	<0.00018	0.0021	<0.00014	0.0003	<0.00017	0.0002
Ce	0.0002	0.0012	0.0009	0.0011	0.0140	<0.00036	0.0076	<0.00029	0.0019	<0.00054	0.0003
Pr	<0.00007	<0.00007	0.0001	<0.00011	0.0013	0.0001	0.0007	<0.00008	0.0004	<0.00009	0.0001
Nd	<0.00043	0.0015	0.0008	<0.00065	0.0058	<0.00055	0.0035	<0.00054	0.0019	<0.00054	0.0006
Sm	<0.00050	<0.00045	0.0004	0.0008	0.0025	<0.00055	0.0012	<0.00067	0.0013	<0.00044	0.0005
Eu	<0.00023	<0.00020	0.0022	0.0003	0.0009	<0.00018	0.0014	0.0002	0.0057	0.0010	0.0002
Gd	<0.00122	<0.00092	<0.00102	<0.00132	0.0040	0.0011	0.0016	0.0012	0.0025	<0.00077	0.0010
Tb	0.0002	0.0002	0.0003	0.0001	0.0006	<0.00012	0.0003	0.0002	0.0004	0.0001	0.0001
Dy	0.0020	0.0024	0.0020	0.0022	0.0033	0.0018	0.0028	0.0017	0.0034	0.0014	0.0003
Ho	0.0007	0.0006	0.0008	0.0007	0.0013	0.0005	0.0007	0.0007	0.0009	0.0006	0.0001
Er	0.0029	0.0032	0.0027	0.0024	0.0046	0.0025	0.0027	0.0024	0.0032	0.0019	0.0002
Tm	0.0007	0.0006	0.0006	0.0004	0.0010	0.0006	0.0006	0.0007	0.0005	0.0004	0.0001
Yb	0.0055	0.0057	0.0050	0.0065	0.0066	0.0048	0.0049	0.0056	0.0053	0.0031	0.0005
Lu	0.0015	0.0014	0.0013	0.0013	0.0016	0.0014	0.0013	0.0013	0.0010	0.0007	0.0001
Hf	0.0009	0.0010	<0.00037	<0.00046	0.0010	<0.00030	<0.00030	<0.00029	<0.00057	0.0003	0.0003
Ta	<0.00017	0.0001	<0.00015	<0.00014	<0.00013	<0.00015	<0.00015	<0.00015	0.0003	<0.00015	0.0001



Table S-11 Silicate glass standard BCR-2 trace element compositions analysed by LA-ICP-MS, in µg/g (or ppm). The deviation relative to the preferred values from GEOREM compilation by Jochum in 01/2009 is reported below.

	Plagioclase First session			Pyroxene First session			Olivine First session			Second session		GEOREM preferred values (1/2009)
Composition (ppm)	BCR-1	BCR-2	BCR-3	BCR-1	BCR-2	BCR-3	BCR-1	BCR-2	BCR-3	BCR-2G-1	BCR-2G-2	BCR-2G
Li	8.12	8.19	7.99	8.1	7.83	8.02	8.64	8.82	8.3	8.83	8.84	9
Mg	18434	18513	17927	26619	26939	27398				34760	34701	21470
Si	246666	246157	245005	247859	247075	247701	255035	255035	255035	263713	264248	254287
Ca	50887	50887	50887	50887	50887	50887	52826	52441	50075	54128	54016	50458
Ti	15256	15434	15326	15245	15072	14884	16032	16161	15326	16096	16239	14100
V	404	420	413	414	402	409	427	437	408	442	449	425
Fe	114427	101960	111879	116470	131338	126848	115206	112244	84804	88528	76745	97221
Sr										335	333	342
Zr	168.78	157.4	162.71	162.47	174.63	164.77	174.3	167.32	165.23	161	158	184
Nb	11.89	12.2	12.02	12.09	11.58	12.1	12.63	12.65	12.51	12.8	12.9	12.5
Ba										711	707	683
La	23.7	22.3	23.3	23.0	23.6	23.1	24.2	23.4	23.5	24.1	23.7	24.7
Ce	47.2	48.7	48.9	48.4	45.8	49.5	50.6	50.7	50.8	53.3	53.3	53.3
Pr	5.74	5.71	5.82	5.79	5.57	5.88	5.99	5.91	6.07	6.41	6.36	6.7
Nd	26.2	25.5	26.4	25.9	25.5	26.6	27.2	26.5	27.4	27.5	27.2	28.9
Sm	6.06	5.82	5.96	5.92	5.99	6.01	6.17	6.03	6.13	6.11	6.06	6.59
Eu	1.71	1.68	1.68	1.67	1.65	1.72	1.75	1.75	1.75	1.80	1.80	1.97
Gd	5.83	5.48	5.70	5.63	5.82	5.74	5.87	5.72	5.79	5.82	5.72	6.71
Tb	0.899	0.847	0.88	0.875	0.901	0.896	0.915	0.889	0.897	0.908	0.890	1.02
Dy	5.76	5.38	5.57	5.55	5.80	5.67	5.82	5.60	5.70	5.60	5.52	6.44
Ho	1.20	1.12	1.17	1.16	1.23	1.20	1.22	1.17	1.20	1.20	1.18	1.27
Er	3.23	2.99	3.10	3.06	3.25	3.14	3.25	3.15	3.17	3.06	3.02	3.7
Tm	0.485	0.454	0.474	0.466	0.496	0.476	0.489	0.476	0.483	0.485	0.479	0.51
Yb	3.06	2.90	3.00	2.94	3.06	3.04	3.10	3.03	3.06	3.04	3.00	3.39
Lu	0.473	0.434	0.455	0.447	0.478	0.475	0.476	0.462	0.469	0.480	0.465	0.503
Hf	4.20	3.91	4.05	4.00	4.25	4.09	4.20	4.09	4.10	3.95	3.87	4.84
Ta	0.689	0.664	0.691	0.672	0.671	0.695	0.703	0.691	0.716	0.717	0.711	0.78



Table S-11 (continued)

Deviation from the reference (%)	Plagioclase First session			Pyroxene First session			Olivine First session			Second session	
	BCR-1	BCR-2	BCR-3	BCR-1	BCR-2	BCR-3	BCR-1	BCR-2	BCR-3	BCR-2G-1	BCR-2G-2
Li	9.8%	9.0%	11.2%	10.0%	13.0%	10.9%	4.0%	2.0%	7.8%	1.9%	1.8%
Mg	14.1%	13.8%	16.5%	24.0%	25.5%	27.6%	100.0%	100.0%	100.0%	61.9%	61.6%
Si	3.0%	3.2%	3.7%	2.5%	2.8%	2.6%	0.3%	0.3%	0.3%	3.7%	3.9%
Ca	0.8%	0.8%	0.8%	0.8%	0.8%	0.8%	4.7%	3.9%	0.8%	7.3%	7.1%
Ti	8.2%	9.5%	8.7%	8.1%	6.9%	5.6%	13.7%	14.6%	8.7%	14.2%	15.2%
V	4.9%	1.2%	2.9%	2.6%	5.4%	3.8%	0.4%	2.7%	4.1%	4.0%	5.6%
Fe	17.7%	4.9%	15.1%	19.8%	35.1%	30.5%	18.5%	15.5%	12.8%	8.9%	21.1%
Sr										2.0%	2.5%
Zr	8.3%	14.5%	11.6%	11.7%	5.1%	10.5%	5.3%	9.1%	10.2%	12.7%	14.3%
Nb	4.9%	2.4%	3.8%	3.3%	7.4%	3.2%	1.0%	1.2%	0.1%	2.6%	3.5%
Ba										4.1%	3.5%
La	4.1%	9.6%	5.9%	6.8%	4.5%	6.5%	2.1%	5.1%	5.0%	2.3%	4.0%
Ce	11.4%	8.7%	8.3%	9.2%	14.1%	7.1%	5.0%	4.9%	4.6%	0.0%	0.1%
Pr	14.3%	14.8%	13.1%	13.6%	16.9%	12.2%	10.6%	11.8%	9.4%	4.3%	5.1%
Nd	9.2%	11.7%	8.8%	10.3%	11.9%	8.1%	5.9%	8.2%	5.3%	5.0%	5.9%
Sm	8.0%	11.7%	9.6%	10.2%	9.1%	8.8%	6.4%	8.5%	7.0%	7.3%	8.0%
Eu	13.3%	14.6%	14.7%	15.1%	16.1%	12.6%	11.2%	11.3%	11.4%	8.7%	8.9%
Gd	13.1%	18.3%	15.1%	16.1%	13.3%	14.5%	12.5%	14.8%	13.7%	13.3%	14.8%
Tb	11.9%	17.0%	13.7%	14.2%	11.7%	12.2%	10.3%	12.8%	12.1%	11.0%	12.7%
Dy	10.6%	16.5%	13.5%	13.8%	9.9%	12.0%	9.6%	13.0%	11.5%	13.0%	14.3%
Ho	5.4%	12.0%	7.7%	8.7%	3.5%	5.3%	4.3%	7.7%	5.7%	5.5%	7.3%
Er	12.7%	19.2%	16.2%	17.3%	12.2%	15.1%	12.2%	14.9%	14.4%	17.3%	18.4%
Tm	4.9%	11.0%	7.1%	8.6%	2.7%	6.7%	4.1%	6.7%	5.3%	4.9%	6.1%
Yb	9.7%	14.5%	11.5%	13.3%	9.7%	10.3%	8.4%	10.5%	9.7%	10.3%	11.5%
Lu	6.0%	13.7%	9.5%	11.1%	5.0%	5.6%	5.4%	8.2%	6.8%	4.6%	7.6%
Hf	13.2%	19.2%	16.3%	17.4%	12.2%	15.5%	13.2%	15.5%	15.3%	18.4%	20.0%
Ta	11.7%	14.9%	11.4%	13.8%	14.0%	10.9%	9.9%	11.4%	8.2%	8.1%	8.8%



Supplementary Information References

- Anders, E., Grevesse, N. (1989) Abundances of the elements: Meteoritic and solar. *Geochimica et Cosmochimica Acta* 53, 197–214.
- Barrat, J.-A. (2004) Determination of parental magmas of HED cumulates: The effects of interstitial melts. *Meteoritics & Planetary Science* 39, 1767–1779.
- Barrat, J.-A., Blichert-Toft, J., Gillet, P., Keller, F. (2000) The differentiation of eucrites: the role of in situ crystallization. *Meteoritics & Planetary Science* 35, 1087–1100.
- Barrat, J.-A., Greenwood, R.C., Verchovsky, A.B., Gillet, P., Bollinger, C., Langlade, J.A., Liorzou, C., Franchi, I.A. (2015) Crustal differentiation in the early solar system: Clues from the unique achondrite Northwest Africa 7325 (NWA 7325). *Geochimica et Cosmochimica Acta* 168, 280–292.
- Barrat, J.-A., Greenwood, R., Keil, K., Rouget, M., Boesenberg, J., Zanda, B., Franchi, I. (2016a) The origin of aubrites: Evidence from lithophile trace element abundances and oxygen isotope compositions. *Geochimica et Cosmochimica Acta* 192, 29–48.
- Barrat, J.-A., Jambon, A., Yamaguchi, A., Bischoff, A., Rouget, M.-L., Liorzou, C. (2016b) Partial melting of a C-rich asteroid: Lithophile trace elements in ureilites. *Geochimica et Cosmochimica Acta* 194, 163–178.
- Bischoff, A., Horstmann, M., Barrat, J.-A., Chaussidon, M., Pack, A., Herwartz, D., Ward, D., Vollmer, C., Decker, S. (2014) Trachyandesitic volcanism in the early solar system. *Proceedings of the National Academy of Sciences* 111, 12689–12692.
- Borg, L., Norman, M., Nyquist, L., Bogard, D., Snyder, G., Taylor, L., Lindstrom, M. (1999) Isotopic studies of ferroan anorthosite 62236: a young lunar crustal rock from a light rare-earth-element-depleted source. *Geochimica et Cosmochimica Acta* 63, 2679–2691.
- Bouvier, A., Spivak-Birndorf, L.J., Brennecka, G.A., Wadhwa, M. (2011) New constraints on early Solar System chronology from Al–Mg and U–Pb isotope systematics in the unique basaltic achondrite Northwest Africa 2976. *Geochimica et Cosmochimica Acta* 75, 5310–5323.
- Bouvier, A., Boyet, M. (2016) Primitive Solar System materials and Earth share a common initial ^{142}Nd abundance. *Nature* 537, 399–402.
- Brown, S.M., Elkins-Tanton, L.T. (2009) Compositions of Mercury's earliest crust from magma ocean models. *Earth and Planetary Science Letters* 286, 446–455.
- Burkhardt, C., Dauphas, N., Tang, H., Fischer-Gödde, M., Qin, L., Chen, J.H., Rout, S.S., Pack, A., Heck, P.R., Papanastassiou, D.A. (2017) In search of the Earth-forming reservoir: Mineralogical, chemical, and isotopic characterizations of the ungrouped achondrite NWA 5363/NWA 5400 and selected chondrites. *Meteoritics & Planetary Science* 52, 807–826.
- Charlier, B., Grove, T.L., Namur, O., Holtz, F. (2018) Crystallization of the lunar magma ocean and the primordial mantle-crust differentiation of the Moon. *Geochimica et Cosmochimica Acta* 234, 50–69.
- Crozaz, G., Floss, C., Wadhwa, M. (2003) Chemical alteration and REE mobilization in meteorites from hot and cold deserts. *Geochimica et Cosmochimica Acta* 67, 4727–4741.
- Day, J.M., Ash, R.D., Liu, Y., Bellucci, J.J., Rumble III, D., McDonough, W.F., Walker, R.J., Taylor, L.A. (2009) Early formation of evolved asteroidal crust. *Nature* 457, 179–182.
- Dhaliwal, J.K., Day, J.M., Corder, C.A., Tait, K.T., Marti, K., Assayag, N., Cartigny, P., Rumble III, D., Taylor, L.A. (2017) Early metal-silicate differentiation during planetesimal formation revealed by acapulcoite and lodranite meteorites. *Geochimica et Cosmochimica Acta* 216, 115–140.
- Dygert, N., Lin, J., Marshall, E.W., Kono, Y., Gardner, J.E. (2017) A low viscosity lunar magma ocean forms a stratified anorthitic flotation crust with mafic poor and rich units. *Geophysical Research Letters* 44, 11,282–11,291.
- Elardo, S.M., Draper, D.S., Shearer Jr, C.K. (2011) Lunar Magma Ocean crystallization revisited: Bulk composition, early cumulate mineralogy, and the source regions of the highlands Mg-suite. *Geochimica et Cosmochimica Acta* 75, 3024–3045.
- Elkins-Tanton, L.T., Burgess, S., Yin, Q.-Z. (2011) The lunar magma ocean: Reconciling the solidification process with lunar petrology and geochronology. *Earth and Planetary Science Letters* 304, 326–336.
- Ferdous, J., Brandon, A., Peslier, A., Pirotte, Z. (2017) Evaluating crustal contributions to enriched shergottites from the petrology, trace elements, and Rb–Sr and Sm–Nd isotope systematics of Northwest Africa 856. *Geochimica et Cosmochimica Acta* 211, 280–306.
- Floss, C., James, O. B., McGee, J. J., & Crozaz, G. (1998) Lunar ferroan anorthosite petrogenesis: Clues from trace element distributions in FAN subgroups. *Geochimica et Cosmochimica Acta* 62, 1255–1283.
- Floss, C. (2000) Complexities on the acapulcoite–lodranite parent body: Evidence from trace element distributions in silicate minerals. *Meteoritics & Planetary Science* 35, 1073–1085.
- Floss, C., Crozaz, G., McKay, G., Mikouchi, T., Killgore, M. (2003) Petrogenesis of angrites. *Geochimica et Cosmochimica Acta* 67, 4775–4789.
- Floss, C., Taylor, L.A., Promprated, P., Rumble III, D. (2005) Northwest Africa 011: A “eucritic” basalt from a non-eucrite parent body. *Meteoritics & Planetary Science* 40, 343–360.
- Gardner-Vandy, K.G., Lauretta, D.S., Greenwood, R.C., McCoy, T.J., Killgore, M., Franchi, I.A. (2012) The Tafassasset primitive achondrite: Insights into initial stages of planetary differentiation. *Geochimica et Cosmochimica Acta* 85, 142–159.
- Goodrich, C.A., Kita, N.T., Yin, Q.-Z., Sanborn, M.E., Williams, C.D., Nakashima, D., Lane, M.D., Boyle, S. (2017) Petrogenesis and Provenance of Ungrouped Achondrite Northwest Africa 7325 from Petrology, Trace Elements, Oxygen, Chromium and Titanium Isotopes, and Mid-IR Spectroscopy. *Geochimica et Cosmochimica Acta* 203, 381–403.
- Guan, Y., Crozaz, G. (2001) Microdistributions and petrogenetic implications of rare earth elements in polymict ureilites. *Meteoritics & Planetary Science* 36, 1039–1056.
- Hibiya, Y., Archer, G.J., Tanaka, R., Sanborn, M.E., Sato, S., Iizuka, T., Ozawa, K., Walker, R.J., Yamaguchi, A., Yin, Q.-Z., Nakamura, T., Irving, A.J. (2019) The origin of the unique achondrite Northwest Africa 6704: Constraints from petrology, chemistry and Re–Os, O and Ti isotope systematics. *Geochimica et Cosmochimica Acta* 245, 597–627.
- Hofmann, A.W. (1988) Chemical differentiation of the Earth: the relationship between mantle, continental crust, and oceanic crust. *Earth and Planetary Science Letters* 90, 297–314.
- Hubbard, N., Gast, P., Meyer, C., Nyquist, L., Shih, C., Wiesmann, H. (1971) Chemical composition of lunar anorthosites and their parent liquids. *Earth and Planetary Science Letters* 13, 71–75.
- Hsu, W., Crozaz, G. (1996) Mineral chemistry and the petrogenesis of eucrites: I. Noncumulate eucrites. *Geochimica et Cosmochimica Acta* 60, 4571–4591.
- Hsu, W., Crozaz, G. (1997) Mineral chemistry and the petrogenesis of eucrites: II. Cumulate eucrites. *Geochimica et Cosmochimica Acta* 61, 1293–1302.



- Hsu, W. (1998) Geochemical and petrographic studies of oldhamite, diopside, and roedderite in enstatite meteorites. *Meteoritics & Planetary Science* 33, 291–301.
- Hyde, B.C., Day, J.M., Tait, K.T., Ash, R.D., Holdsworth, D.W., Moser, D.E. (2014) Characterization of weathering and heterogeneous mineral phase distribution in brachinite Northwest Africa 4872. *Meteoritics & Planetary Science* 49, 1141–1156.
- Jochum, K. P., Weis, U., Schwager, B., Stoll, B., Wilson, S. A., Haug, G. H., Andreae, M.O., Enzweiler, J. (2016) Reference values following ISO guidelines for frequently requested rock reference materials. *Geostandards and Geoanalytical Research* 40, 333–350.
- Jones, T.H. (1995) Experimental trace element partitioning. In: Ahrens, T.J. (Ed.) *Rock Physics and Phase Relations: A Handbook of Physical Constant, AGU Reference Shelf 3*, 83. American Geophysics Union, Washington DC, 73–104.
- Koefoed, P., Amelin, Y., Yin, Q.-Z., Wimpenny, J., Sanborn, M.E., Iizuka, T., Irving, A.J. (2016) U–Pb and Al–Mg systematics of the ungrouped achondrite Northwest Africa 7325. *Geochimica et Cosmochimica Acta* 183, 31–45.
- Kong, P., Su, W., Li, X., Spettel, B., Palme, H., Tao, K. (2008) Geochemistry and origin of metal, olivine clasts, and matrix in the Dong Ujimqin Qi mesosiderite. *Meteoritics & Planetary Science* 43, 451–460.
- Lin, Y., Tronche, E.J., Steenstra, E.S., van Westrenen, W. (2016) Evidence for an early wet Moon from experimental crystallization of the lunar magma ocean. *Nature Geoscience* 10, 14–18.
- Martin, D., Nokes, R. (1989) A fluid-dynamical study of crystal settling in convecting magmas. *Journal of Petrology* 30, 1471–1500.
- Lodders, K. (1998) A survey of shergottite, nakhlite and chassigny meteorites whole - rock compositions. *Meteoritics & Planetary Science* 33, A183–A190.
- Norman, M.D., Borg, L.E., Nyquist, L.E., Bogard, D.D. (2003) Chronology, geochemistry, and petrology of a ferroan noritic anorthosite clast from Descartes breccia 67215: Clues to the age, origin, structure, and impact history of the lunar crust. *Meteoritics & Planetary Science* 38, 645–661.
- Osborn, E.F. (1942) The system CaSiO₃–diopside–anorthite. *American Journal of Science* 240, 751–788.
- Palme, H., Spettel, B., Wänke, H., Bischoff, A., Stöffler, D. (1984) Early differentiation of the Moon: Evidence from trace elements in plagioclase. *Journal of Geophysical Research: Solid Earth* 89, C3–C15.
- Papike, J.J., Fowler, G.W., Shearer, C.K., Layne, G.D. (1996) Ion microprobe investigation of plagioclase and orthopyroxene from lunar Mg-suite norites: Implications for calculating parental melt REE concentrations and for assessing postcrystallization REE redistribution. *Geochimica et Cosmochimica Acta* 60, 3967–3978.
- Papike, J., Fowler, G., Shearer, C. (1997) Evolution of the lunar crust: SIMS study of plagioclase from ferroan anorthosites. *Geochimica et Cosmochimica Acta* 61, 2343–2350.
- Patzner, A., Hill, D.H., Boynton, W.V. (2004) Evolution and classification of acapulcoites and lodranites from a chemical point of view. *Meteoritics & Planetary Science* 39, 61–85.
- Phinney, W., Morrison, D. (1990) Partition coefficients for calcic plagioclase: Implications for Archean anorthosites. *Geochimica et Cosmochimica Acta* 54, 1639–1654.
- Shaw, D.M. (1970) Trace element fractionation during anatexis. *Geochimica et Cosmochimica Acta* 34, 237–243.
- Schosnig, M., Hoffer, E. (1998) Compositional dependence of REE partitioning between diopside and melt at 1 atmosphere. *Contributions to Mineralogy and Petrology* 133, 205–216.
- Snyder, G.A., Taylor, L.A., Neal, C.R. (1992) A chemical model for generating the sources of mare basalts: Combined equilibrium and fractional crystallization of the lunar magmasphere. *Geochimica et Cosmochimica Acta* 56, 3809–3823.
- Spivak-Birndorf, L.J. et al. (2015) Geochemistry and chronology of the Bunburra Rockhole ungrouped achondrite. *Meteoritics & Planetary Science* 50, 958–975.
- Stelzner, T.H., Heide, K., Bischoff, A., Weber, D., Scherer, P., Schultz, L., Happel, M., Schrön, W., Neupert, U., Michel, R., Clayton, R.N., Mayeda, T.K., Bonani, G., Haidas, I., Ivy-Ochs, S., Suter, M. (1999) An interdisciplinary study of weathering effects in ordinary chondrites from the Afer region, Algeria. *Meteoritics & Planetary Science* 34, 787–794.
- Suckale, J., Elkins - Tanton, L.T., Sethian, J.A. (2012) Crystals stirred up: 2. Numerical insights into the formation of the earliest crust on the Moon. *Journal of Geophysical Research: Planets* 117, E08005.
- Swindle, T., Kring, D., Burkland, M., Hill, D., Boynton, W. (1998) Noble gases, bulk chemistry, and petrography of olivine - rich achondrites Eagles Nest and Lewis Cliff 88763: Comparison to brachinites. *Meteoritics & Planetary Science* 33, 31–48.
- Vander Kaaden, K.E., McCubbin, F.M. (2015) Exotic crust formation on Mercury: Consequences of a shallow, FeO-poor mantle. *Journal of Geophysical Research: Planets* 120, 195–209.
- Wadhwa, M., Shukolyukov, A., Davis, A., Lugmair, G., Mittlefehldt, D. (2003) Differentiation history of the mesosiderite parent body: Constraints from trace elements and manganese-chromium isotope systematics in Vaca Muerta silicate clasts. *Geochimica et Cosmochimica Acta* 67, 5047–5069.
- Weber, I., Morlok, A., Bischoff, A., Hiesinger, H., Ward, D., Joy, K., Crowther, S., Jastrzebski, N., Gilmour, J., Clay, P. (2016) Cosmochemical and spectroscopic properties of Northwest Africa 7325 – A consortium study. *Meteoritics & Planetary Science* 51, 3–30.
- Wheelock, M.M., Keil, K., Floss, C., Taylor, G.J., Crozaz, G. (1994) REE geochemistry of oldhamite-dominated clasts from the Norton County aubrite: Igneous origin of oldhamite. *Geochimica et Cosmochimica Acta* 58, 449–458.
- Yamaguchi, A. et al. (2001) Post-crystallization reheating and partial melting of eucrite EET90020 by impact into the hot crust of asteroid 4Vesta~ 4.50 Ga ago. *Geochimica et Cosmochimica Acta* 65, 3577–3599.
- Yang, J., Zhang, C., Miyahara, M., Tang, X., Gu, L., Lin, Y. (2019) Evidence for early impact on hot differentiated planetesimal from Al-rich micro-inclusions in ungrouped achondrite Northwest Africa 7325. *Geochimica et Cosmochimica Acta* 258, 310–335.

